PHASE UNWRAPPING AND INVERSION RESOLUTION OF INTERFEROMETRIC SYNTHETIC APERTURE RADAR GEODESY

A Thesis

Presented to the Faculty of the Graduate School

of Cornell University

in Partial Fulfillment of the Requirements for the Degree of

Master of Science

by

Philip Nee

August 2012

ABSTRACT

We use Interferometric Synthetic Aperture Radar (InSAR) data to examine surface deformation in the Imperial Valley, California, with the goal of further constraining the fault geometry and along-strike variations in slip behavior of the Imperial fault. 48 Interferograms are created from 38 European Space Agency (EAS) Envisat ASAR acquisitions, spanning 7 years. We observe extensive agriculture activities in the Imperial Valley, and geothermal and groundwater related subsidence. However, no prominent tectonic deformation signals can be identified in the valley due to 1: Poor-quality InSAR data due to extensive agricultural activity, and 2: the lack of GPS measurements at the spatial and temporal densities required to fully characterize behavior of the Imperial fault.

Due to technical difficulties of InSAR, spatial variation in data density in the Imperial valley greatly affects our data quality and numerical resolution. To ensure our results are robust, we perform synthetic tests to examine the numerical resolution and data quality of a given data set. The results can later be used as quality assessments and validation for our results. The point-target identification method that allow us to extract the stable pixels from interferogram time series as well as approaches for masking out less stable areas so that they do not contaminate our results in the rest of the region, is also being tested. In the case study, we examine deformation across the Superstition Hills Fault and a deformation source near the Salton Sea, potentially caused by geothermal activities. The vicinity near the Superstition Hills fault is deforming at peak velocity of ~8mm/yr, revealing a prominent fault trace, and the geothermal deformation is moving at ~6mm/yr, both rates taken in the direction of the satellite line-of-

sight (LOS).

ACKNOWLEDGEMENTS

It has been a wonderful experience to have come to Cornell University for graduate study. I have seen myself mature, personally and intellectually, in this stimulating learning environment for the past two years. I learned great science and modesty here, and I cannot express my excitement for being a part of this academic community. I met fantastic people and many of them are, and will be meaningful for rest of my life. I owe much to friends and family, especially to my advisor, Professor Rowena B. Lohman, for her support, suggestions, and encouragements. Her wealth of knowledge has been invaluable for the course of this degree.

I must thank my undergraduate advisor, Professor Gareth J. Funning from University of California at Riverside, who introduced me to the world of space geodesy and taught me much about radar Interferometry and geophysics.

I thank William Barnhart (Bill), Chen Chen (cc), Jennifer Jay, Andrew K. Melkonian, Scott Henderson, Anastasia Cabolova, Diego Quiros, Nicolàs Cosentino, TianQi Liu, Chao Shi, YJ Chen from Department of Physics, Yun-Ru Chen from Boyce Thompson Institute, and Charlie Chan from Department of Computer Science for their friendship, and fellow graduate/undergraduate students. Special thank to Yao Li for her companionship. She enriches my life outside of the world of science.

I acknowledge and thank my committee member, Professor Rick Allmendinger for his suggestions and time reviewing this material.

I thank Professor Matt Pritchard for organizing our weekly group meeting, and provides many constructive suggestions to my researches.

Lastly, I thank my parents and my sister for their love and understanding. This thesis is impossible without them.

I acknowledge NSF grant 0911464 for supporting my M.S. research project.

To my parents. J. B. Nee and Jing-Lin Chang

TABLE OF CONTENTS

LIST OF FIGURES

CHAPTER 1

INTRODUCTION

We attempt to refine our knowledge about earthquake rupture dynamics to further improve the current hazard assessments in the seismically active areas around the world. Many methods have been used to study the dynamics of rupture processes, such as seismology, geodesy, and paleo-seismology. However, regions that are poorly instrumented, do not have sufficient data resolution to provide useful constrain on physical models. For example, the geological structures in our study region in the Salton Trough, i.e., the Imperial Fault system, are poorly constrained due to the lack of near field instrumentations and details of the fault geometry and characteristics of previous ruptures. In order to improve data coverage, particular in our study region, we use an advanced space-borne geodetic technique, Interferometric Synthetic Aperture Radar (InSAR), to examine the surface deformation of the San Andreas Fault (SAF), with particular interest in the southern end of the fault system.

The spreading center between the Pacific Plate and Farallon Plate, also known as the East Pacific Rise, began interacting with the trench separating the Farallon Plate and the North American Plate at about 30Ma (Figure 1.1). Subduction of the East Pacific Rise near the current location of the city of Los Angeles resulted in a new right-lateral transform boundary forming between the Pacific Plate and North American Plate, which has become one of the longest continental transform plate boundaries, the San Andreas Fault (SAF). The SAF runs approximately 1,300 km from the Mendocino Triple Junction to the Imperial Valley in the South. The relative motion between the North American Plate and Pacific Plate accommodated by the SAF varies along strike, typically

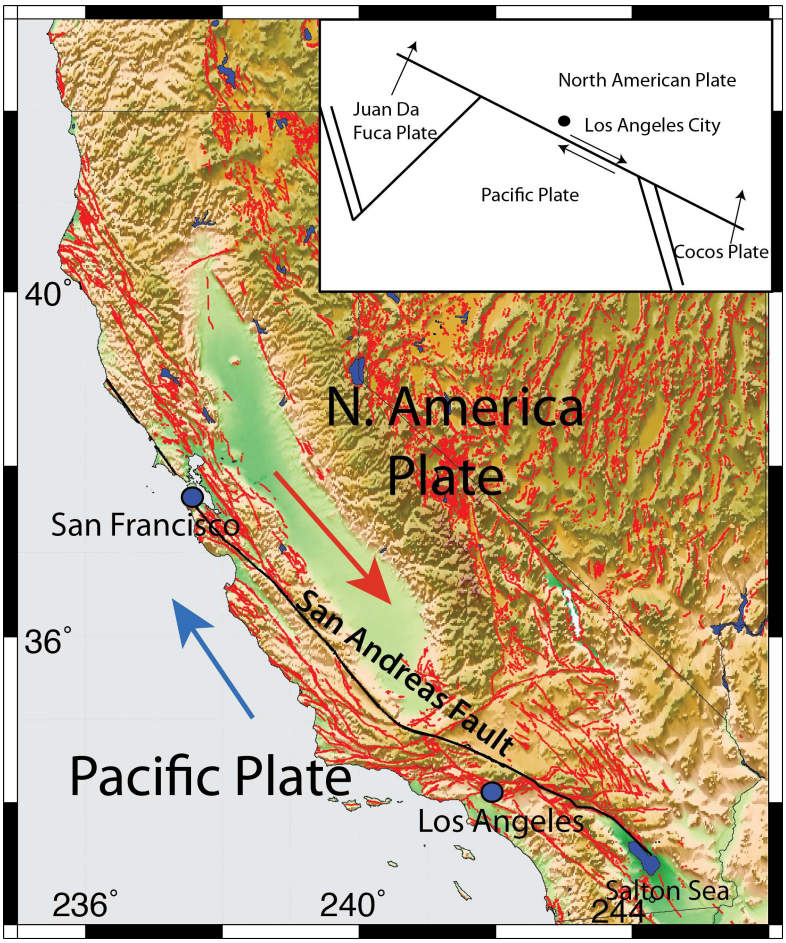

Figure 1.1: Tectonic setting of California. San Andreas Fault (SAF) is the right-lateral plate boundary between North American Plate and Pacific Plate. The red arrow indicates the proximate moving direction of the North America Plate, and the blue arrow indicates the proximate moving direction of the Pacific Plate. Red lines are the known faults, and the black line is the current location of the San Andreas Fault.

~40mm/yr for the current 3Ma (*C. DeMets, l R. G. Gordon and Stein* (1994)).

The southernmost segment of the SAF system, i.e. the Salton Trough and the Imperial Valley, spans the transition between the strike-slip San Andreas Fault system and the oceanic spreading system in the Gulf of Mexico (Figure 1.1). The SAF terminates near the Salton Trough, and many fault systems in the vicinity, e.g., the Imperial Fault and the Superstition Hills Fault, have similar sense of motion (right-lateral strike slip) and can be explained as an extension of the SAF system (Figure 1.2).

The Imperial Valley, located in the south of the Salton Sea, has year-round agriculture activities sustained by irrigation from Colorado River. The area also experiences subsidence due to ground water discharge/recharge, high heat flow and magmatic anomalies (*Kerrick et al.* (1995)), and higher level of seismicity than the rest of the California, e.g. *Brune and Allen* (1967); *Hill et al.* (1975). Faults within the Imperial Valley exhibit a wide range of behaviors; including medium size earthquakes, such as the 1940 and 1979 Mw 5.9 and 6.4 earthquakes along the Imperial Fault, triggering events (e.g., *Glowacka et al.* (2002)), shallow fault creep (e.g.,*Lyons et al.* (2002)), and seismic swarms (e.g.,*Lohman and Mcguire* (2007)).

Realizing the needs to improve our understanding of tectonic behavior, i.e., the geometry, seismic and mechanical behavior of this fault system, we conduct this survey to examine the surface deformation of the region and further understand the physical behavior of the SAF. The potential seismic hazard of this region is also of interest due to lack of record of large earthquakes in the region for the past 300 years along the segment of the San Andreas Fault immediately to the north of the Imperial Valley Fault (*Smith-Konter and Sandwell* (2009)). Our

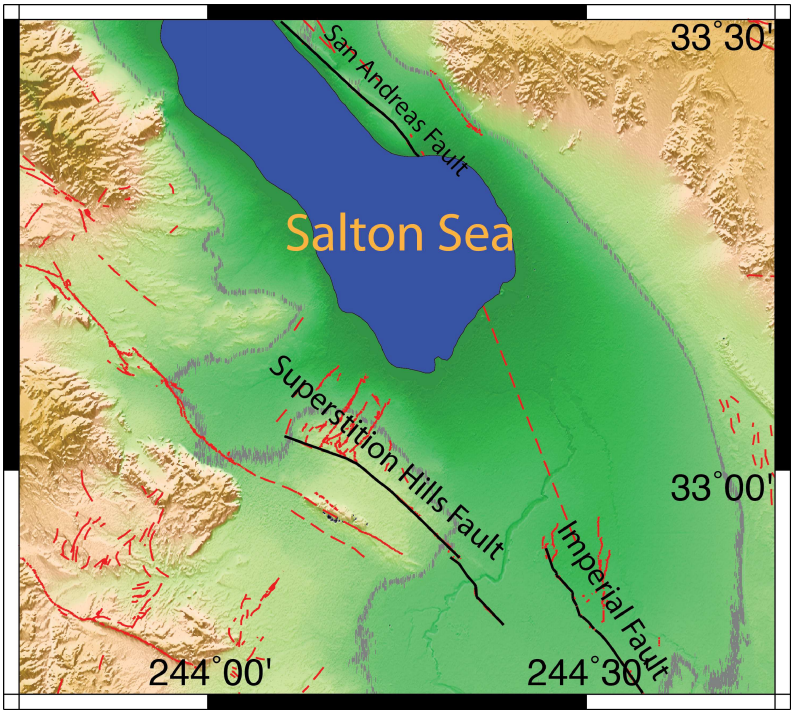

Figure 1.2: Map of the Imperial Valley. The water body is the Salton Sea, and area to the south of Salton Sea is the Imperial Valley. The Imperial Fault runs through the valley. The Superstition Hills Fault is the fault trace to the West of the Imperial Fault. Red lines indicate the known faults and the black lines are the San Andreas Fault, the Imperial Fault, and the Superstition Hills Fault, each is labeled by the adjacent texts.

case study, through understanding the strain accumulation of the fault system, may lead to explanations for the lack of large earthquakes along the Southern SAF system. Our results can improve understanding of how strain is accommodated by the main segment as well as transferring of slip to the neighboring faults, and/or released via aseismic creep.

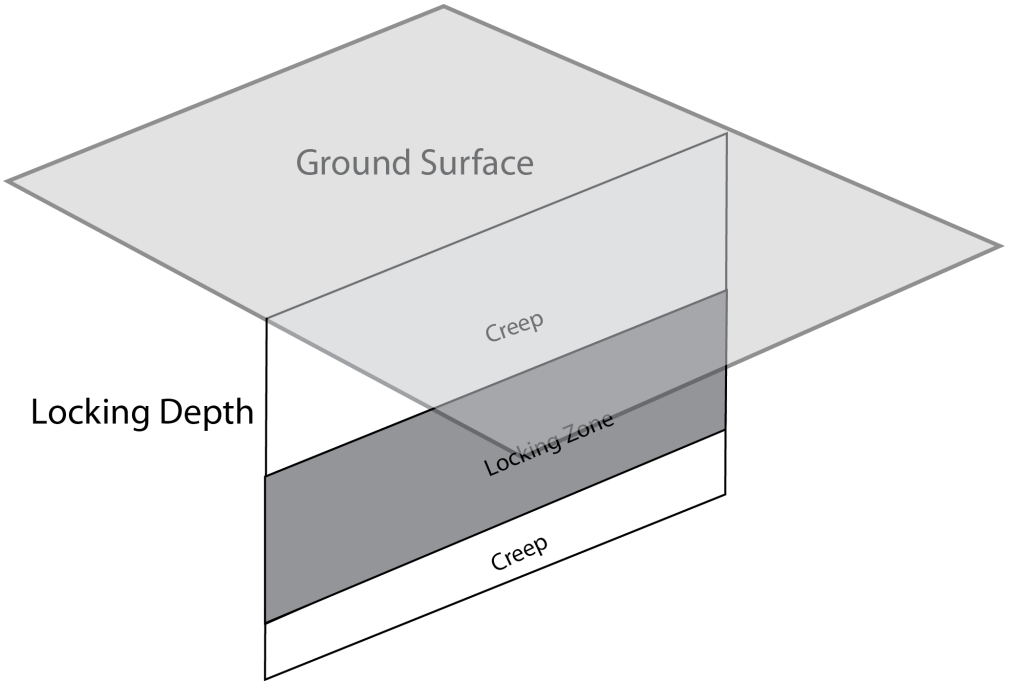

Figure 1.3: Schematic of a fault in half-space. This figure demonstrates how an active deforming fault can have a locking depth. The locking depth is the distance from the surface to the depth where no slip occurs. In the figure, the grey region is locked and only slip during coseismic events.

The case study examines the behavior of faults within the Imperial Valley, with a focus on using InSAR to observe surface deformation caused by tectonic events. Most geophysical observations suggest the Imperial Fault has a shallow locking depth and is actively deforming. *Thomas and Rockwell* (1996), suggest that deformation rates across the Imperial Fault are ~15mm/yr for the past 300 years based on sedimentary records, whereas Global Positioning System

(GPS) data (*Bennett et al.* (1996) , *Meade and Hager* (2005)) suggest rates closer to ~40mm/yr with locking depth between 7.5-10km. Seismological data suggests a locking depth of 7-10 km (*Shearer* (2002)), and seismic refraction surveys suggest that the depth of the basement interface is at ~12km. Our goal here is to produce an improved physical model that can adequately explain most of the observations. Our model is derived based on Interferometric Synthetic Aperture Radar (InSAR) data, taking the advantage of its dense spatial coverage. Eventually, this information will lead to better understanding of the evolution of stress state near the southern end of the SAF and how stresses related to large-scale plate motion are accommodated in the fault system. Our study will also have several practical applications such as understanding large-scale fault mechanics and earthquake hazard assessment.

InSAR is a satellite-based geodetic technique that allow us to study surface deformation over broad areas (~100 km). The spatially dense coverage (~20 meter pixels) of InSAR data, also known as interferograms, is particularly useful for study of fine scale deformation features on the fault that might be missed by even the densest campaign or continuous GPS deployments. However, the temporal coverage is much sparser than the coverage that can be achieved with continuous GPS, with time periods between acquisitions typically spanning a month or more. Therefore, InSAR data is complementary to the traditional on-site surveying methods, e.g. GPS, leveling and strainmeters.

In this study, we find that interferograms within the Imperial Valley are heavily contaminated by deformation due to extensive agriculture activities and variations in atmospheric water vapor; therefore, the interferograms in their most standard form are of such low quality that they provide little constraint

on fault behavior within the Valley. Here, I explore new approaches for preconditioning the data in order to improve the results. These approaches include masking of the noisiest regions of the data, the examination of full time-series of data rather than just single interferograms, and extensive synthetic tests that allow us to determine the limitations of the various techniques. The deformation time series here is constructed using the Small-BAseline-Subset approach (SBAS) (*Berardino et al.* (2002)). I also demonstrate our initial results on data spanning the Superstition Hills Fault.

1.1 Introduction to Interferometric Synthetic Aperture Radar

Interferometric Synthetic Aperture Radar (InSAR) is a remote sensing technique utilizing satellite images to map the relative deformation between two acquisitions. It is a very robust geodetic survey method due to the large spatial extent and centimeter precision achievable by the data. In this chapter, I review the basic concepts of InSAR and some technical details of radar interferometry. I first discuss the fundamental principle of InSAR and describe the signal characteristics. I then present a generic functional model for InSAR data, and review some potential errors sources. The Appendix, includes a flow chart for InSAR processing strategies.

1.1.1 Interferometric Synthetic Aperture Radar

Synthetic Aperture Radar (SAR) was initially designed to survey the planetary surface using the amplitude of backscattered microwave. The concept of SAR

interferometry was first discussed by *Richman* (1971) and *Zisk* (1972), but only became suitable for geodetic survey purposes in the past 20 years, due to increases in computational capacity and the launches of space-borne SAR platforms such as the European Remote Sensing satellite, ERS-1 in 1991, followed by ERS-2 launched in 1995.

SAR platforms are equipped with an active antenna, transmitting and receiving at microwave wavelengths. The antennae are side-looking, typically, right-looking. The acquisition of an image can be either along the ascending (South to North) portion of the orbit or descending (North to South) (Figure 1.4).

Unlike conventional optical remote sensing, the microwave wavelengths used in SAR can be operated in all weather, and day/night conditions (optical remote sensing for example, cannot penetrate clouds). Electromagnetic waves can be characterized by their amplitude and phase angle. Amplitude in our data is controlled by the electromagnetic properties of the surface of the ground target, and phase angle is controlled by the distance between the satellite and ground target, as well as anything affecting the propagation of microwaves through the space in between. The core concept of InSAR relies on utilizing the differential phase angle from two images to constrain ground target displacements. The spatial distance between the satellite locations at two acquisitions is the spatial baseline, and the time separation is referred to the temporal baseline (Figure 1.5). The processes involved in generating an interferogram are described in the following section.

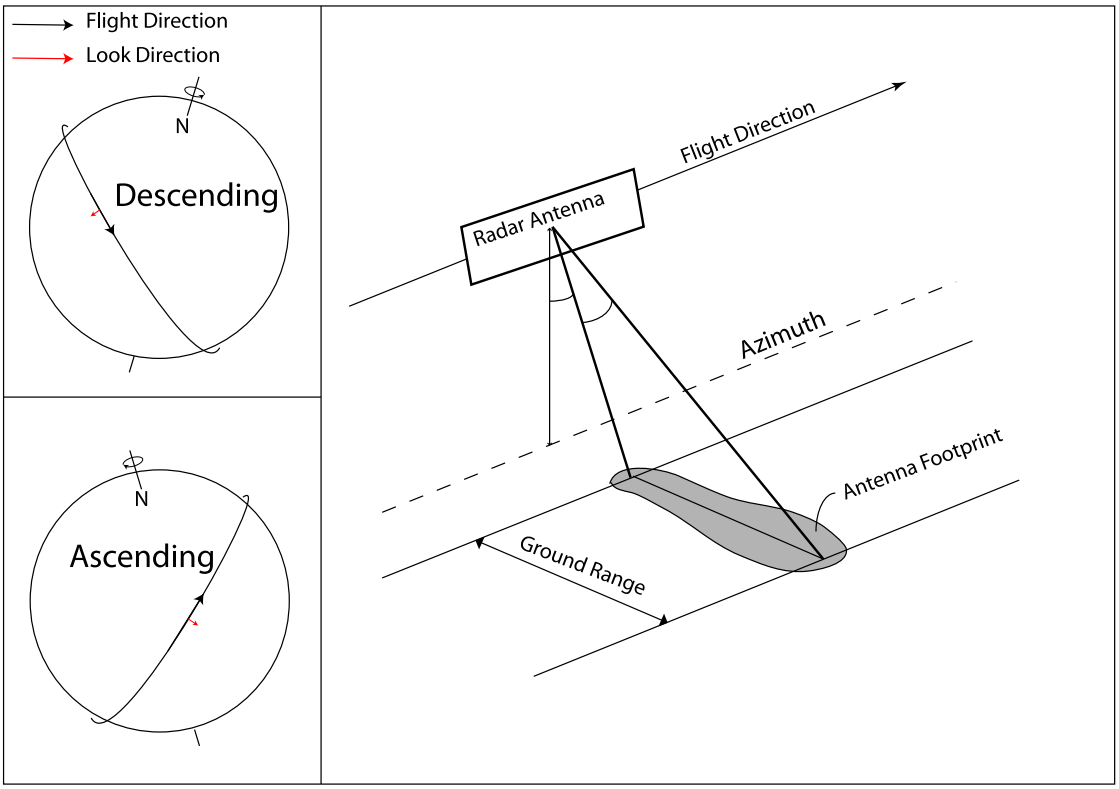

Figure 1.4: Schematic of satellite look geometry. Space-borne SAR platforms are side looking, in order to avoid the directional ambiguity that would occur if they were pointed in the nadir direction. The azimuth direction is defined as being along the flight track, and the range direction is perpendicular to the flight direction.

1.1.2 Interferogram Formation

Several steps are typically required to produce an interferogram, i.e. data conditioning, image coregistration, interferometry, and several post-processing steps. A general processing flow is described in the Appendix. In this section, I briefly describe the key steps involved in performing SAR interferometry.

Data conditioning (formation of Synthetic Aperture): The Synthetic Aperture Radar concept synthesize multiple, overlapping transmissions from a small an-

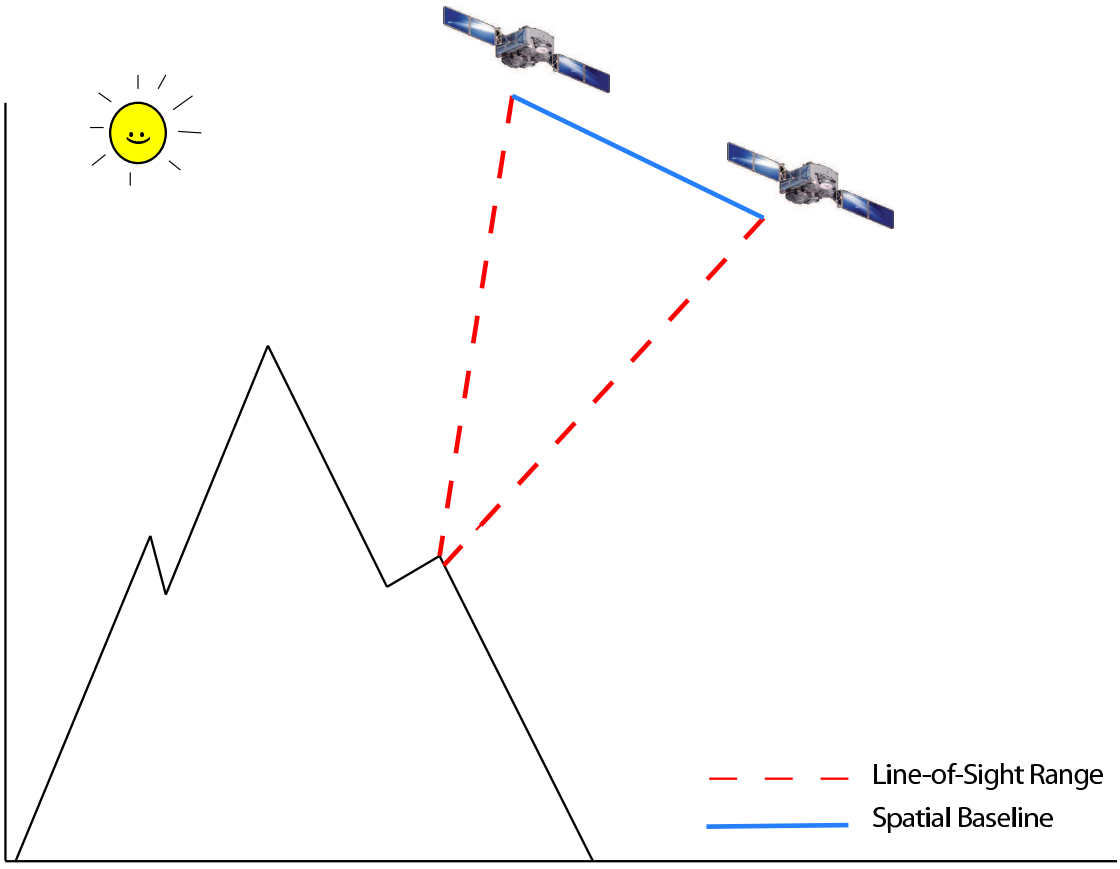

Figure 1.5: Two acquisitions of data covering the same ground pixel from different positions. The red dashed lines are the "line-of-sight" look directions. In reality, the satellites are far enough away that these vectors are near-parallel. The blue line is the spatial baseline, or the spatial separation between two acquisitions. The locations of the two acquisitions are almost never the same due to drift of satellite's orbit.

tenna to emulate similar effect of a large antenna array, such that the spatial resolution can be much improved. However, since the data are acquired on a moving platform, we need to account for the Doppler effect in azimuth direction (in flight direction). This process is typically referred to imagery focusing, and we obtain the Single-Look Complex (SLC) from this step.

Image coregistration: After the two SAR images are focused, sub-pixel coreg-

istration is required prior to performing interferometry at full resolution. To ensure pixels from one acquisition are the correspondence to the other image, amplitude information is used to correlated two images via a normalized cores-correlation process, since we expect the reflection properties will no change significantly between the two acquisitions. After coregistration is performed, we can compute the relative transformation between two images, and register and rectify the one image into the geometry of the other image, defining the latter as the master image and the other as the slave image, using such transformation information.

Interferogram formation: After coregistration, we can then generate an interferogram representing the pixel-to-pixel complex multiplication, as it is shown in the following formula:

$$I_{master-slave} = I_{master} I^*_{slave} = |A_{master}||A_{slave}| \exp^{j(\phi_{master}-\phi_{slave})} \tag{1.1}$$

where I_{master} and I_{slave} represent the master and slave images. $I_{master-slave}$ is the interferogram obtained after complex multiplication, A_{master} and A_{slave} are the image amplitude, and ϕ_{master} and ϕ_{slave} are the phase angle of master and slave images.

Post-processing: After the raw interferogram is obtained, we correct for the regional topography, errors due to orbital imprecision, and perform noise filtering. At this stage, all data are in module 2π format, a.k.a. wrapped. Next we perform phase unwrapping , to convert all wrapped data to continuous deformation signals (Described further in Chapter 2). After all data are properly

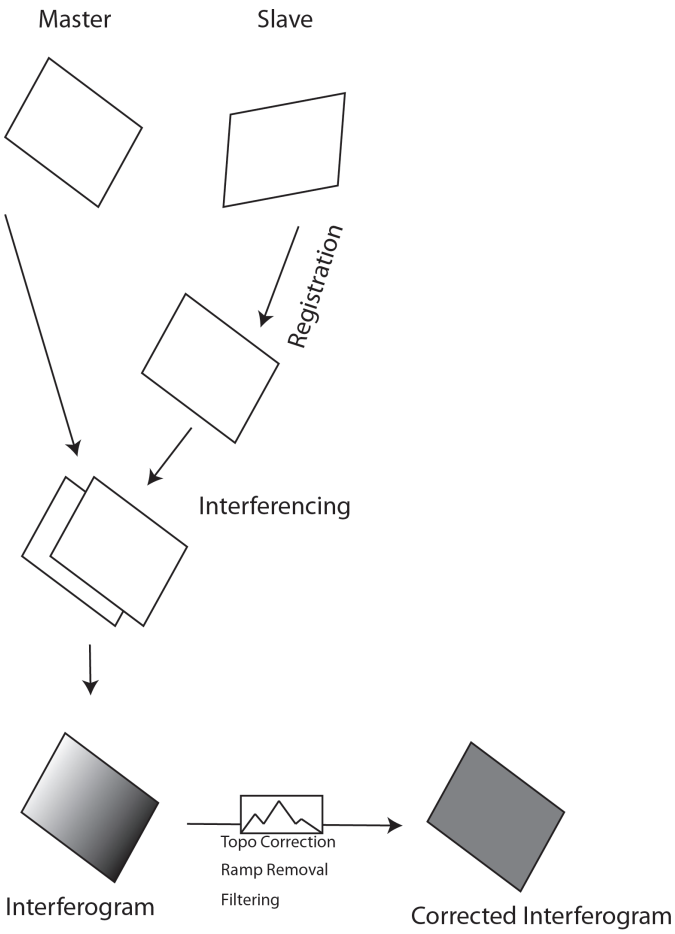

Figure 1.6: Differential InSAR uses two SAR acquisitions to produce an interferogram. The slave image is registered to the master scene, then transformed into the geometry of the master image. After the initial interferogram is produced, topography and orbital ramp are modeled and removed.

unwrapped, we convert our data into geographic coordinates. This step is often referred to as geocoding, and the final product is the geocoded interferogram.

The geocoded interferogram is the final product of the InSAR process, the image itself however, can be heavily contaminated by different noise sources, each of which is described in the following section. Depending on the condition and signal-to-noise ratio (SNR) of the unwrapped data, we typically need to ap-

ply treatments to our data to estimate the noise and improve the measurements.

1.2 Generic Functional Model

An interferogram is the sum of contributions from deformation signals, atmospheric delay, topography, and several other error terms (*Zebker et al.* (1992), *Zebker and Villasenor* (1992)]. The model can be written in the following mathematic formulation, and each term is defined in the following:

$$\Psi = \sum \varphi_{def} + \varphi_{topo} + \varphi_{atm} + \varphi_{orbit} + \varphi_{noise} \tag{1.2}$$

φ_{def} is the phase contribution due to surface deformation signals. Our goal is to accurate estimate this term.

φ_{topo} is the phase contribution due to inaccuracy of the reference DEM. The phase is a linear function of perpendicular baseline between two acquisitions as described the following formulation:

$$\varphi_{topo} = -\frac{4\pi}{\lambda}\frac{B_{\perp}^{0}}{R_k \sin\theta^0} H_k \tag{1.3}$$

where λ is the wavelength, $B_{\perp}$ is the baseline, R_k is the range of line-of-sight, θ^0 is the incident angle, and H_k is the topographic height. The topographic phase is proportional to the perpendicular baseline; therefore, having a large perpendicular baseline results in a strong topographic signal.

φ_{atm} is the atmospheric delay due to water vapor and atmospheric stratifi-

cation. The structure of this signal is typically correlated with distance, but the character of this correlation changes within the image (i.e., the signal is not isotropic or stationary). A positive or negative correlation with topography also generally exists, due to the vertical layering of water vapor in the atmosphere.

φ_{orbit} is the phase contribution due to inaccuracy of the estimated satellite locations. Since variations to the satellite orbit happen over large distances, the signal tends to have a large spatial scale and can be characterized as a linear ramp in the simplest manner, or an nth-order polynomial ramp. In the future sections, ramp removal is referred to removing the orbital phase.

φ_{noise} is the phase contribution from signal decorrelation (see section 1.3). Levels of decorrelation vary, in our case study in the Imperial Valley our data suffers strong decorrelation from several sources, including the existence of water, agriculture and movement of sand dunes. One of the goals of this thesis is to use several techniques to reduce the impact of decorrelation, such as time series methods, data masking, and filtering. In the subsequent section, I identify several sources of decorrelation.

1.3 Sources of Decorrelation

Signal decorrelation occurs when the phase values from pixel to pixel begin to look like uniformly distributed noise ranging from 0 to 2π. If phase variation of the signal is larger than half a cycle (or π) between neighboring pixels, the phase angle appear to be spatially random, and the signal is decorrelated. Sources of decorrelation are vast (e.g.*Zebker et al.* (1992)), here I briefly discuss some important sources:

1) *Baseline decorrelation* Baseline decorrelation is caused by a large difference in incidence angle between the two acquisitions (i.e., a large baseline). Above a critical baseline, the geometry is such that the phase change from pixel to pixel with increasing range is greater than π. Additionally, large variations in incidence angle result in the actual scattering targets appearing differently between the two images, with different phase behaviors so that essentially you are observing a different set of scatterers.

2) *Temporal decorrelation* Temporal decorrelation occurs if the surface of the ground target varies too much over the time spanning two acquisitions. For example, surface change due to farming, vegetation growth, and seasonal snow cover or the short time-scale changes that occur over any water body can become major sources of temporal decorrelation.

3) *Topographic decorrelation* Topographic decorrelation is caused by foreshortening and layover effects due to the non-vertical look angle and high topographic relief, as well as baseline-dependent decorrelation in regions of high relief..

4) *Doppler decorrelation* Large differences in Doppler centroid between two acquisitions result in differences in pixel geometry and cause decorrelation.

5) *Others* Other sources of decorrelation include thermal noise from the instruments, processing decorrelation from coregistration, and decorrelation caused by a vertical distribution of scatterers such as is found in regions with tree cover.

CHAPTER 2

PHASE UNWRAPPING: FUNDEMENTALS AND SOME NUMERICAL ASPECTS

2.1 Introduction

Improving the accuracy of deformation measurements using Interferometric Synthetic Aperture Radar (InSAR) is one of the most important areas of ongoing research in the field of space geodesy. The error embedded in our data, as described in our functional model (see section 1.2), is a combination of atmospheric delays due to water vapor, satellite orbital errors, errors in the digital elevation model (DEM), and phase unwrapping errors. Most of these terms are difficult to model due the complexity of nature; therefore Improving approaches to mitigate and estimate all of these errors are very important, yet being very difficult. This chapter is fully dedicated to the sources of error due to phase unwrapping because of the large impact of such errors on interferograms in the Imperial Valley.

In this chapter, I will introduce the theoretical aspects of phase unwrapping and its application to InSAR. I first review several existing unwrapping algorithms and identify their potential limitations. I then present results from tests using synthetic data, which form the basis of the study in the Imperial Valley, California.

The synthetic tests presented later in the chapter are designed to provide quality assessment for our results using the Imperial Valley data. In this study, we use the Statistical-Network cost flow algorithm, Snaphu (*Chen and Zebker*

(2002)), as our primary phase unwrapping approach since it produces robust results for many cases. However, Snaphu, like all unwrapping algorithms, still has difficulties in regions with a great deal of noise. Therefore, I also explore a range of approaches for implementing the Snaphu algorithm, e.g., masking and weighting of low-quality data, to examine any potential improvements. The synthetic tests designed for this case study should be useful for evaluating other cases where phase unwrapping may be challenging.

2.2 Principles of Phase Unwrapping

In many scientific and engineering disciplines, data involving electromagnetic waves includes measurements of the complex state of the wave, or of the magnitude and phase of the wave at a particular time. Interferometry also results in data that is recorded in complex format, i.e., it cycles between π and π, due to the nature of electromagnetic waves. The true signal, which may range over many cycles, is said to be wrapped to values that are the remainder after dividing the full value by 2π, also referred to as the modulo 2π value. Phase unwrapping is the attempt to reconstruct the true, unwrapped signal from the wrapped interferogram.

Due to the cyclical nature of electromagnetic waves, reconstructing the actual unwrapped signal from the modulo 2π observation (wrapped) is difficult because an infinite number of signals could be wrapped to the same set of values. Therefore, correctly estimating the unwrapped phase offsets becomes one of the most important topics in InSAR research.

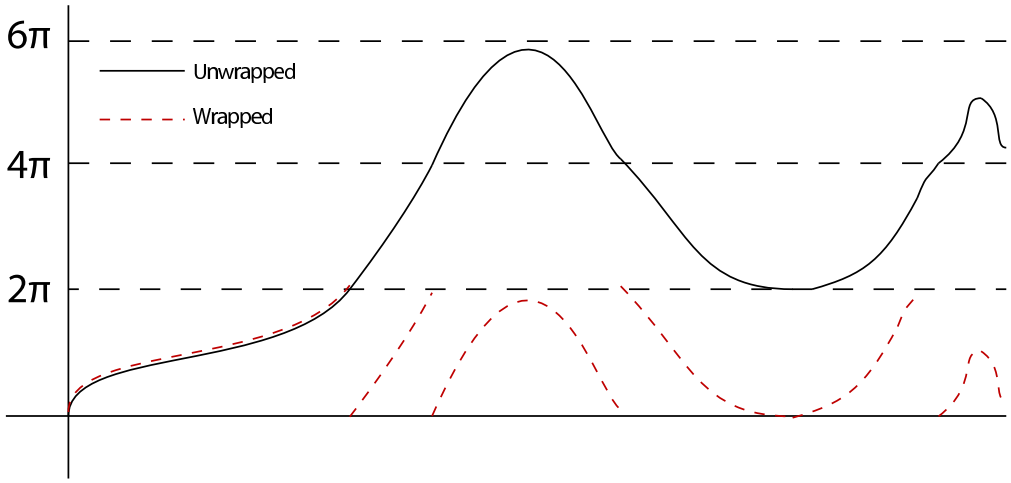

Figure 2.1: A comparison of the unwrapped and wrapped signal in 1D. Black solid line is the continuous unwrapped solution, and red dashed line is the wrapped version

2.3 Phase Unwrapping in 1-D Phase Unwrapping in 1-D

The difficulties of phase unwrapping mainly come from the lack of a priori knowledge about the original unwrapped data. Phase unwrapping is essentially a highly non-unique problem, since any numbers of 2π cycles added to the data can produce the same wrapped signal observed (Figure 2.1); therefore, the problem can only be addressed by applying constraints on the desired unwrapped solution.

As it is shown in Figure 2.1, the unwrapped phase information is not necessarily lost completely during phase wrapping. The slope of the wrapped and unwrapped data is identical except when there is an abrupt 2π jump in the data. If we are able to estimate the locations of these phase jumps and the number of cycles that need to be added at these points, we can recover the original unwrapped signal. The most common assumption used in phase unwrapping is

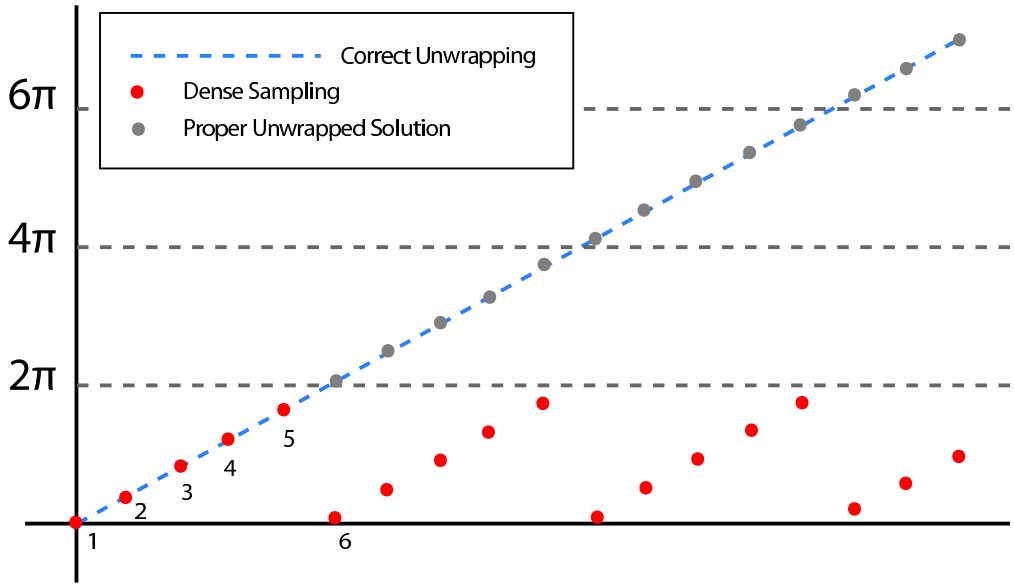

Figure 2.2: Example of phase unwrapping. Phase can be properly restored (the blue dashed line and the grey dots) when sampling is spatially dense (red dots).

that the true unwrapped phase should not vary more than $\frac{1}{2}$ cycle between any two neighboring pixels. This is similar to assuming that the pixel size in the interferogram is small enough that sampling of the unwrapped signal satisfies the Nyquist criterion. In cases where the signal is very complex, such as if the deformation gradient is high or there is a great deal of topography, this assumption can break down. In the following figure, I demonstrate how phase unwrapping using this assumption proceeds in 1-D. In Figure 2.2, the blue dashed line is the original continuous unwrapped signal. When this signal is sampled at the grey dots and wrapped to 2π, we obtain the red dots. The key to unwrapping the signal is to look at the phase difference between neighboring pixels. We obtain an unwrapped solution by first computing the phase differences of the adjacent pixels, integrating the value along a chosen direction, and adding or subtracting 2π whenever the phase difference between adjacent pixels exceed π. For exam-

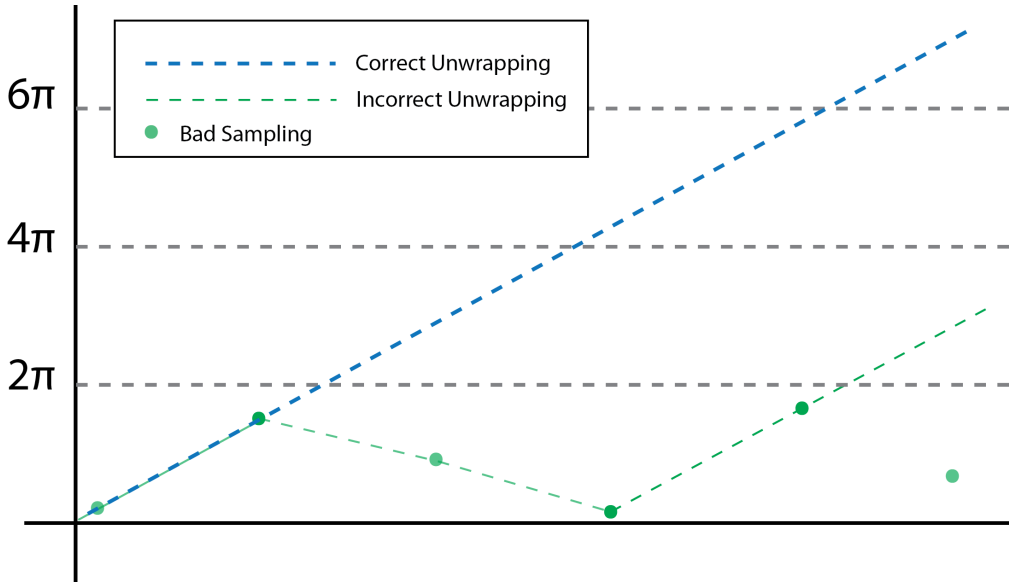

Figure 2.3: As the sampling frequency becomes too low, phase unwrapping fails. Colors as in Figure 2.2..

ple, in Figure 2.2, the sum of the phase differences between pixel 1 through 5 are less than one cycle (2π), but the sum exceeds π going from pixel 5-6. Therefore, one cycle is added to the rest of the segment from pixel 6 onwards. Figure 2.3 demonstrates how phase unwrapping becomes impossible if spatial sampling rate is too sparse. Here, the green dots in figure 2.3 are inadequately sampled from the original signal and key information about the signal is missing; therefore, the correct unwrapped solution is impossible to recover. The algorithm described above will not result in the correct solution. Another case where phase unwrapping may fail in 1-D is when actual phase differences between pixels are more than π. This may be due to large amounts of noise, signals with high strain gradients, high topographic relief, etc. Here, it is demonstrated in one example in the following figure.

In 2.4, the wrapped signals (blue lines) can be unwrapped into both red and

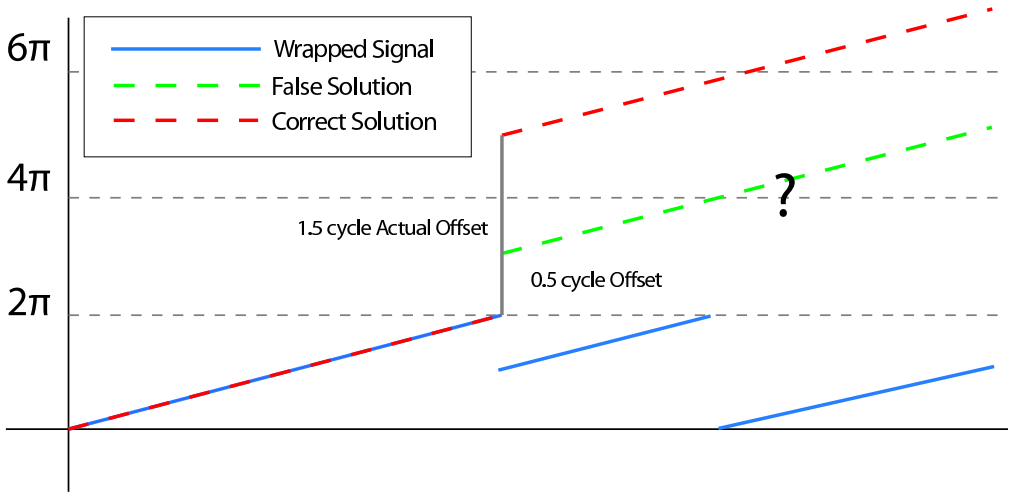

Figure 2.4: This figure demonstrates that it is impossible to obtain the correct solution if the actual offset exceeds 2π, since the potential solutions are non-unique and infinite.

green dashed line. For scenarios like this, if the actual offset is over one cycle, it is impossible to solve in 1-D since the process is highly non-unique (red and green dashed line can be wrapped into the same signal). However, with additional phase information in both horizontal and vertical directions in 2-D, the correct solution can be obtained.

2.4 Phase Unwrapping in 2-D

In the previous section, I demonstrated how 1-D phase unwrapping can be performed by integration of phase differences for every adjacent data point and the addition of 2π jumps whenever the phase difference between adjacent pixels exceeds π. In 2-D, phase unwrapping can also be performed in a very similar manner; instead of computing line integrals, we compute a closed path integral and attempt to identify integration paths that cross boundaries where 2π needs to be

added/subtracted. Addition of dimensionality introduces more complexity to the problem, but it also allows better constraints on the solution. Before exploring 2-D unwrapping, we must first describe some key features in 2-D wrapped signals. Wrapped 2-D signals contain continuous boundaries of 2π offsets that bound regions belonging to the same phase cycle. Here I define these regions as *equi-cycle* surfaces, and the boundaries of phase offsets are defined as *equi-cycle* contours.

In 2-D, wrapped data can contain many *equi-cycle* contours, and our objective here is to identify the locations of those contours and to determine the proper numbers of 2π cycles that need to be added to the surfaces embedded in these contour lines in order to reconstruct the true, wrapped data. In Figure 2.5, I illustrate the original unwrapped signal can be wrapped into multiple *equi-cycle* planes.

In 1-D unwrapping, the simple algorithm of adding a 2π jump whenever the phase difference between adjacent pixels is greater than π breaks down in regions where the true unwrapped phase signal is not smooth or has a steep gradient. Similarly, in 2-D, we must identify regions where the characteristics of the signal are such that simply integrating the phase differences along a path and adding or subtracting 2π jumps will reproduce the true signal. To do this, we can compute closed loop integrals of wrapped phase differences along arbitrary paths in the wrapped interferogram. Whenever the absolute value of the phase difference is $> \pi$, it is wrapped itself by adding or subtracting 2π. If the closed loop integral is zero, then the path crosses an equal number of negative and positive jumps and ends up on the same *equi-cycle* surface that it started on; if the integral has a value of +/- some multiple of 2π, then we know that we have

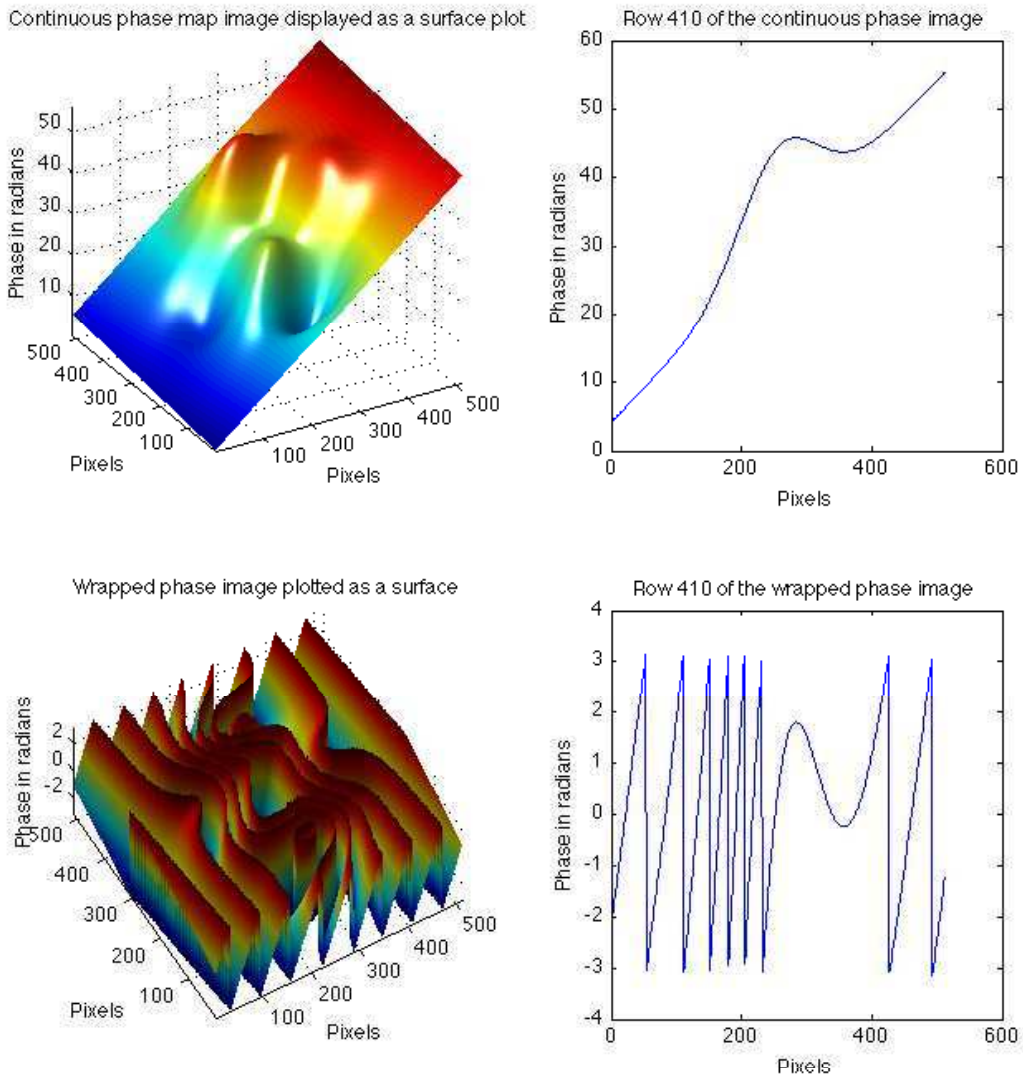

Figure 2.5: Demonstration of wrapped and unwrapped signal in 2-D. The vertical axis is the pixel value in radians. The unwrapped signal has values ranging from 0 to 3 radians, the unwrapped signal ranges between [$-\pi$,π]. The phase profiles to the right show the phase values for row 410, plotted with distance along the profile.

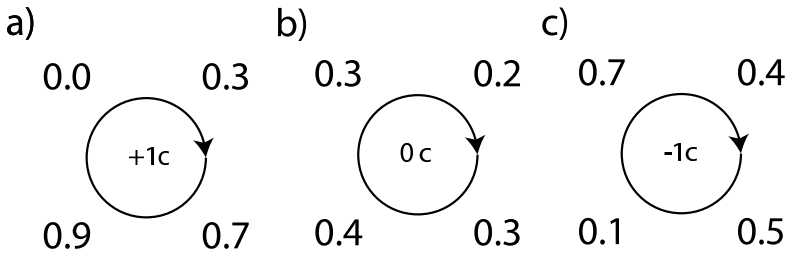

Figure 2.6: Identification of residues in 2D phase unwrapping (values indicate number of cycles, not radians). The residual is computed by summing the wrapped phase differences between pixels around a 2x2 box in a clockwise direction.

crossed an unbalanced number of positive and negative *equi-cycle* contours. This path is then described as having either a positive or negative residue (*Goldstein and Werner* (1998)). This is demonstrated in the following figure, where all values have been divided by 2π. In (a), if we start at the upper left, the wrapped phase differences are: 0.3 − 0.0 = 0.3, 0.7 − 0.3 = 0.4, 0.9 − 0.7 = 0.2 and 0.0 − 0.9 = − 0.9, which is then wrapped to 0.1. Therefore, the sum is 0.3 + 0.4 + 0.2 + 0.1 = 1 cycle. This indicates that the loop between these four pixels cross one *equi-cycle* contour in an upwards direction, but does not cross back down before reaching its starting point.

2.4.1 The Residual-Cut/Branch-cut algorithm

Goldstein and Werner (1998) proposed a method for estimating the unwrapped phase by computing the residue for clockwise sums of phase differences around all sets of four adjacent cells for the entire image (see section 2.4). As it is discussed earlier, residues can be zero, positive or negative, depending on the set of *equi-cycle* contours that they cross.

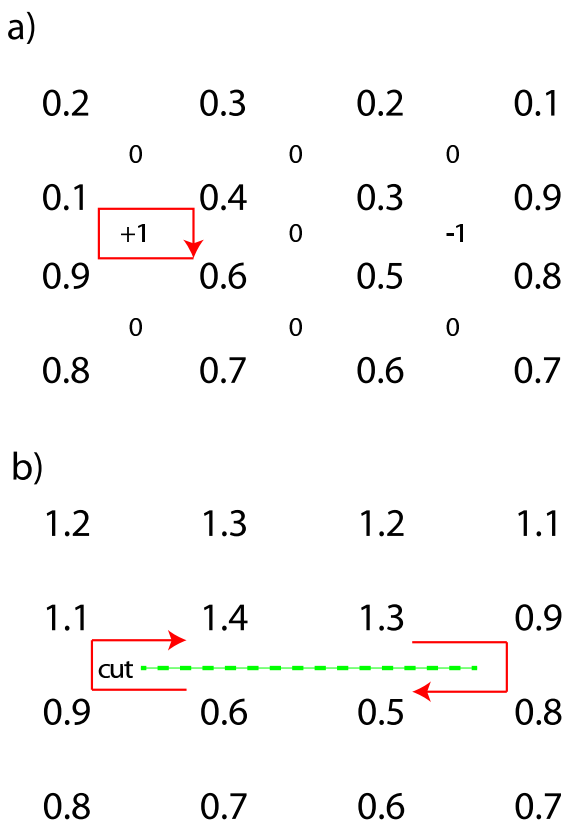

Figure 2.7: a) The raw signal in fractions of a cycle with the residue computed for each 4-cell loop. b) The unwrapped solution after a cut is made between the -1 and +1 residual.

In Figure 2.7, the residue is computed in all four-cell loops in an image as it is described in Figure 2.6. After computing the residual for the entire data set, lines referred to as branch-cut are generated between pairs of +1 and −1 residues Figure 2.7 b). When the algorithm finally begins to unwrap the data in the same way as one would unwrap 1-D data, by integrating the phase differences along a path (often simply traveling along rows or columns in a sequential manner) and adding or subtracting 2π whenever the phase jumps exceeded π, the integration path is chosen so that it never crosses any of these branch cuts. Approaches for selecting the tree of branch cuts vary, but tend to attempt to minimize either the number or length of branches required to connect all pairs of residues in the

image. Residues near the edge of the image can be connected by a branch to the side of the image if necessary.

The algorithm fails in regions with significant decorrelation because the residue density becomes so dense that it is impossible to come up with suitable trees of branch cuts, or because regions of coherent data are completely separated from each other by decorrelated regions. In cases when two regions are disrupted by a gap (such as would be found for an island near the mainland), we need to manually estimate the phase jump between two regions and connect them, sometimes by using a known displacement between the two regions (e.g., from GPS data), or by choosing a 2π offset between the two that minimizes the total unwrapped phase gradient within the interferogram as a whole. For example, in the Imperial Valley, California, the residual-cut algorithm performs poorly in all but interferograms spanning the shortest time intervals (1 month or less), due to extensive decorrelation within the valley. However, we observe many small correlated regions (such as cities like El Centro) connected by coherent paths within the valley (usually roads or dry riverbeds), and it is theoretically possible but very time-intensive to exploit these coherent paths and manually unwrap the interconnected coherent regions that are each themselves unwrapped with the residue-cut algorithm. Here we will instead focus on the use of the much less labor-intensive approach discussed in the next section.

2.4.2 Statistical-Cost Flow Algorithm: Snaphu

Chen and Zebker (2001) proposed the Statistical-cost, Network-flow Algorithm (Snaphu) an algorithm follow the Lp framework proposed by *Ghiglia and Romero*

(1994). Both algorithms conceptually, search for solutions that minimize global cost (here global means the whole image) with L-p norm criteria:

$$min\{\sum_{i,j} w_{i,j}^{(x)}|\Delta\phi_{i,j}^{(x)} - \Delta\varphi_(i,j)^{(x)}|^p + \sum_{i,j} w_{i,j}^{(y)}|\Delta\phi_{i,j}^{(y)} - \Delta\varphi_(i,j)^{(y)}|^p\} \tag{2.1}$$

Here, $\Delta\phi$ and $\Delta\varphi$ are the phase gradients of wrapped and unwrapped phases of each pair of pixels, and i,j are the indices for vertical and horizontal directions. p is the penalization parameter (2, for least-squares), and $w^{(x)}$ and $w^{(y)}$ are the weight functions in the x and y direction. The conceptual meaning of this equation is to minimize the weighted phase gradient between wrapped and unwrapped signal, globally (the summation notation). For regularly gridded data, $^{(x)}$ and $^{(y)}$ indicate the column and row phase gradient, respectively. The cost function cost function in this context is essentially the logarithm of the probability density function of the unwrapped phase gradient under the assumption that it should be spatially smooth but still be consistent with the observed, wrapped phase gradients. In other words, minimizing cost function maximizes the a posteriori probability of the unwrapped solution. The optimum solution can obtain through different iterative nonlinear algorithms. The details are described in *Chen and Zebker* (2001).

In the context of this thesis, we use Snaphu for unwrapping our data, both real and synthetic, due to its robustness in many settings and the fact that it does not need manual interaction; however, unwrapping full resolution interferograms that contain a large amount of noise and decorrelation is far too computationally expensive. Therefore, we typically unwrap the data after a large amount of spatial averaging, also known as looking-down.

Our data in the Imperial Valley, California, is comprised of extensive decorrelation due to agriculture activity. Our goal is first, to unwrap across the valley using the connecting coherent pixels, and second, to unwrap the isolated coherent patches such as cities, stable ground objects, correctly, in order to recover the deformation field caused by the deforming faults in the vicinity of our data coverage.

2.5 Motivation and Objective of 2-D Synthetic Tests

The residual-cut method becomes unfeasible for use in our case study in the Imperial Valley due to extensive decorrelation in the agriculture regions within the valley (Figure 2.8). Our goal is to use our a priori knowledge about which features in the interferogram are the most coherent to improve phase unwrapping in the valley using Snaphu. For instance, we would ideally condition the problem so that the algorithm does not spend any time or place any weight on the unwrapped result within the Salton Sea itself, which we expect to be completely incoherent. Two approaches that we explore here are where we weight or mask the data before unwrapping, and where we use a point-target unwrapping approach described below.

To validate our different unwrapping approaches, we generated synthetic data with known signal and noise structure, and varied characteristics of the signal, noise, and correlation to see how the various unwrapping techniques performed. Unlike in the real-world scenario, our synthetic tests allow us to determine exactly when the unwrapped solution differs from the true solution. Our experimental cases in this chapter are designed to improve our understand-

ing of the potential error sources in the Imperial Valley, California, as well as allowing us to choose the best possible unwrapping approach for this setting. Therefore, our synthetic data are targeted to simulate the Imperial Valley, California environment, with levels of noise and signal characteristics that are similar to what we find in the real data. Nevertheless, our results also contribute to the general problem of how to effectively unwrap data in various situations, and provide a qualitative assessment of' the potential problems that might affect phase unwrapping.

In this section, I first examine how well Snaphu can unwrap different characteristic signals, i.e. noise, spatially correlated signals, signals with linear phase gradients (similar to the ramp found in many interferograms), and combinations of those. I then discuss different weighting and masking approaches and their success in reproducing the true signal for our synthetic tests.

2.5.1 Gaussian White Noise on 2D Regular Grid

We begin by generating different levels of white noise on a regular data grid and then wrap them. In each case, we then unwrap the signals using Snaphu. We expect Snaphu to be able to recover the original unwrapped signal perfectly if the noise level is sufficiently low, and to result in more errors as the noise increases. We define error as the difference between the true signal before wrapping, and our final, unwrapped signal. For each pixel, this difference will be some multiple of 2π.

In Figure 2.9, the noise is lowest (1σ = 0.05 cycle) in the left most figure (and highest (1σ=0.5 cycle) in the right most. The phase variation in the leftmost

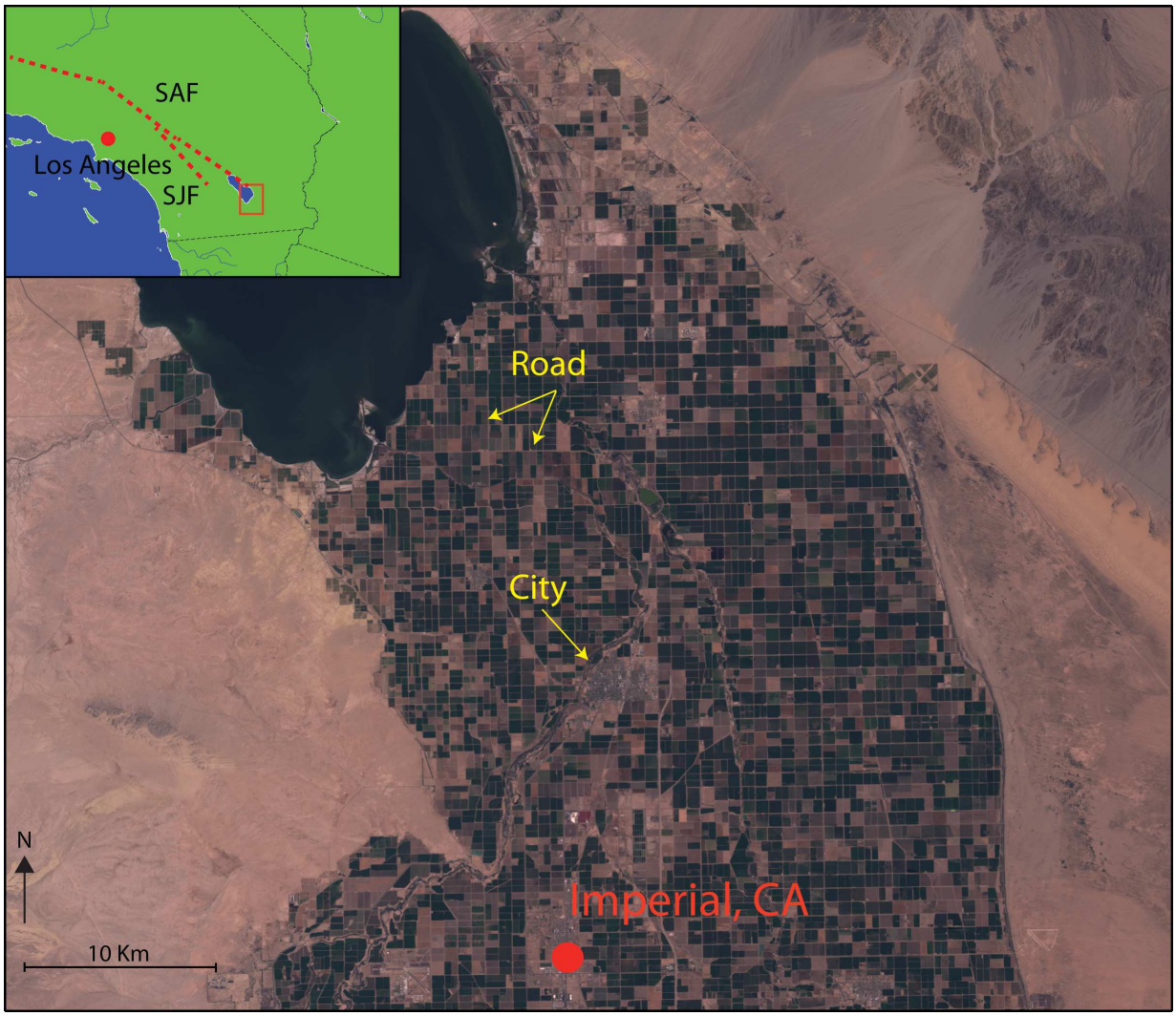

Figure 2.8: Landsat optical imagery (Combination of Band 1, 2, 3) covering the Imperial Valley, California. The Salton Sea is located in the southern end of the San Andreas fault (SFA). The San Jacinto Fault (SJF) (see inset) accommodates a fraction of strain from the SAF system, but is not covered by this image. The yellow arrows indicate the roads and cities that can be used to improve unwrapping of the InSAR data.

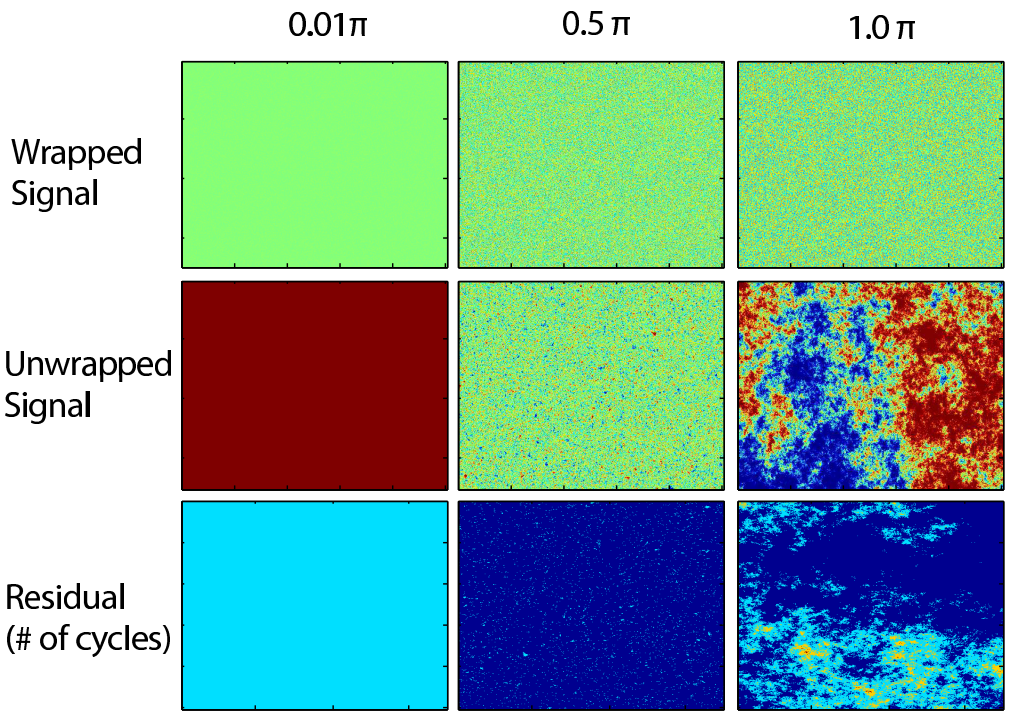

Figure 2.9: Top three panels are the input wrapped data at 3 different noise levels, the middle three panels are the output unwrapped signals, and the bottom three are the residual. Residual is defined as the difference between the input signal before wrapping and the output, unwrapped signal.

column (lowest noise) should be unwrapped perfectly, and rightmost column (highest noise)is impossible to unwrap due to high phase variation. Note that the residual in the leftmost column has a consistent 1 cycle (2π) residual across the entire image. Since unwrapping has an ambiguity in the absolute number of cycles that are added to the entire image, this sort of constant offset is just as good of an unwrapping result as if the residual were 0 across the entire image. The low noise residual in Figure 2.9 has 0 cycle difference for almost all pixels, and high noise residual shows significant unwrapping errors across the image.

To systematically examine the performance of phase unwrapping using Snaphu, we unwrap 10 different sets of noise at each noise level. To assess the

errors, we cannot simply examine the magnitude of the residual between the wrapped and unwrapped values, since we sometimes find examples where the output is successfully unwrapped except for a 2π offset of the entire unwrapped product (which, as we describe above, would not be considered a poor result), or a single unwrapping error that results in half of the image being correct and the other half being off by 2π. Instead, we require a metric that would penalize these two scenarios much less than one where $+/-2\pi$ offsets were scattered across the entire result. To do this, we compute the normalized cross-correlation value between the input and unwrapped output as our quality assessment. This metric would result in a correctly unwrapped product that just happened to have a multiple of 2π added to the entire image being assessed as being just as good as one where the unwrapped product was exactly equal to the input. Here I perform the normalized cross-correlation between the input unwrapped signals and the unwrapped solution by Snaphu. I examine central cross-correlation values, which is value comparing pixel to pixel. In following figure, I compute the cross-correlation value for increasing white noise level, as it is described in Figure 2.10. As we increase the noise level, the cross-correlation drops as we expect.

2.5.2 Spatially Correlated Noise : Simulated Atmospheric Delay Signals

The white noise that we used in the previous example is, perhaps, an unrealistically difficult type of noise to use in tests of phase unwrapping. For white noise, the phase gradients between pixels can be very high even if the overall

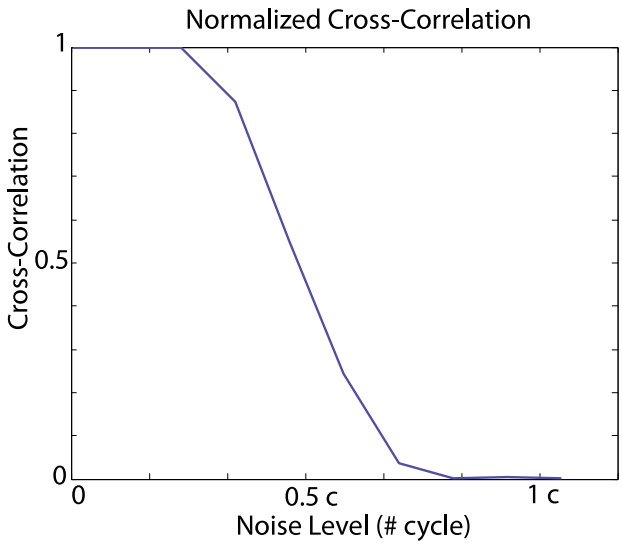

Figure 2.10: Cross-correlation value vs. white noise level, averaged over 10 trial runs for each noise level. The unwrapping errors become progressively larger as we increase the noise level (cross-correlation value gets smaller).

noise level is not large. In general, interferograms tend to contain spatially correlated atmospheric delay signals, which have much lower gradients of noise between pixels. It is very difficult to fully characterize the noise signals found in real InSAR data by any currently existing mathematical models; however, we typically describe it as a stationary, isotropic signal where correlation between pixels decays with distance (*Emardson, T. R.* (2003)). Realistic noise can be generated by using a length-scale dependent covariance matrix (Figure 2.11) - the covariance between any pair of pixels diminishes exponentially or logarithmically with distance.

However, this method becomes computationally expensive for large numbers of data points (>10,000 pixels) since the memory required to store the covariance matrix is number of points to the fourth power! An alternative way to compute atmospheric delay signal is to generate a set of white noise

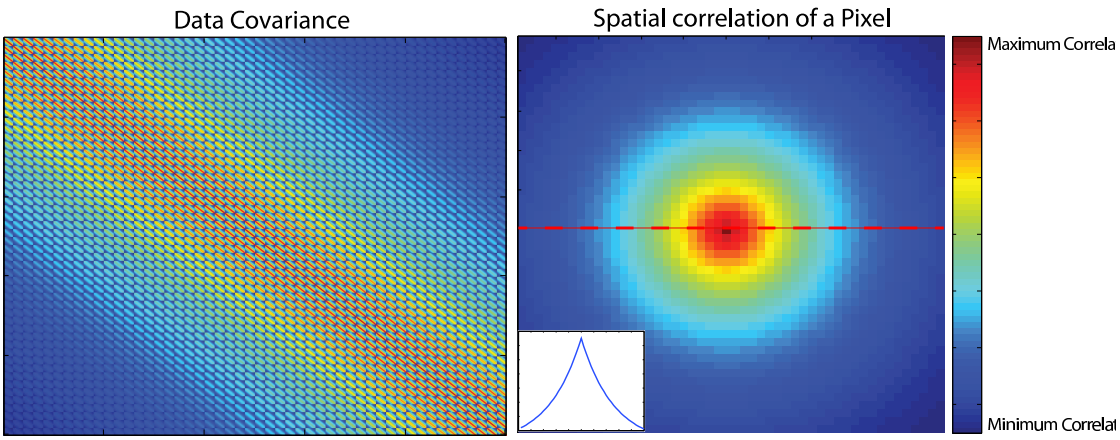

Figure 2.11: Data covariance matrix for our synthetic atmospheric delay signal (left). Each row represents the correlation between a particular pixel and all other pixels in the image. Values on the diagonal represent the variance of each pixel. The figure to the right is the contribution from a single pixel in the center of the image, corresponding to one row of the full covariance matrix. Notice that the magnitude of contribution decreases exponentially with distance from the pixel itself. The inset in the lower left corner is the profile of correlation vs. distance across the red dashed line.

and then filter it so that the power spectral density matches what is found in typical studies of atmospheric noise (Figures 2.11and 2.12) (Peter Kovesi, www.csse.uwa.edu.au/~pk). The data covariance structure (Figure 2.13) is very similar to the previous method.

Here I combine synthetic white and spatially correlated noise as our input data set. To focus on the effects of spatially correlated noise, I make the normally distributed white noise level very low (+/- 0.2 π). I vary the spatially correlated (atmospheric) signal level and compare the unwrapped solution to the input in the same way as was done in the previous section. In Figure, the left-most column has the lowest phase variation (1σ=0.05 cycle), and the right most column has the highest phase variation (1σ= 1.5 cycle). Since the signal is spatially

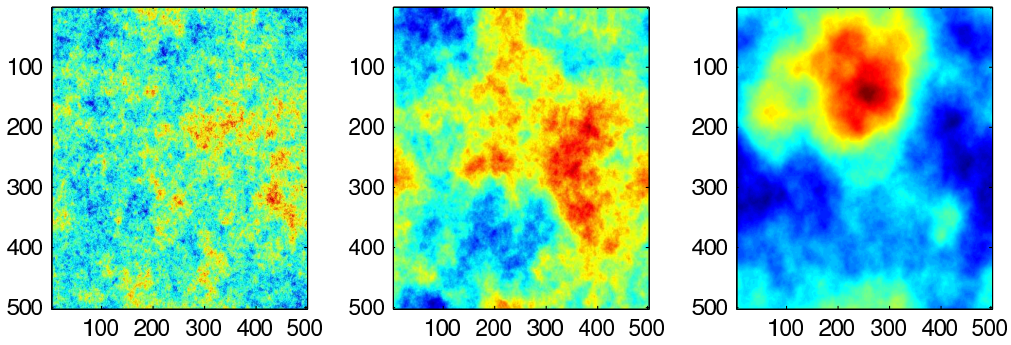

Figure 2.12: Atmospheric noise generated by the spectral method. Different scale factors provide different scale of correlation. We find the most realistic atmospheric noise can be generated using 1.3-1.5.

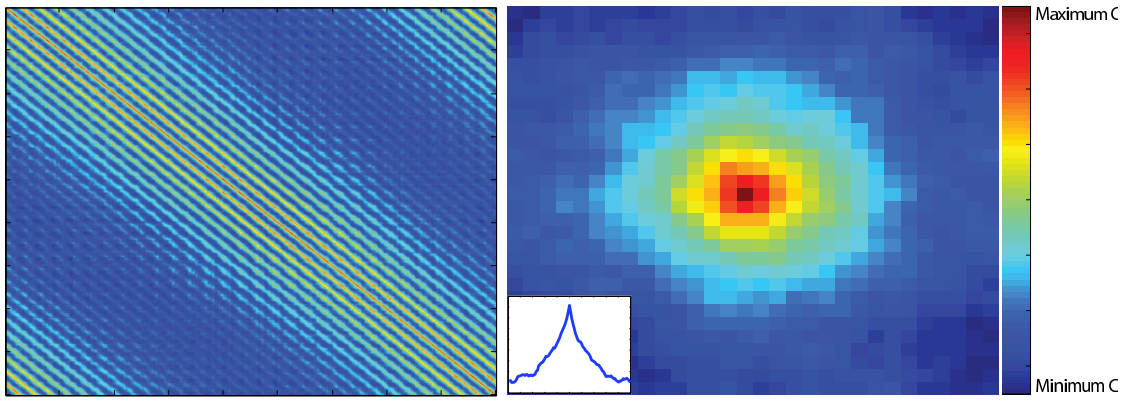

Figure 2.13: Covariance structure of our atmospheric signal, generated by creating 500 sets of noise using the Kovesi approach. The left figure (data covariance matrix) shows a symmetric structure for each data point, since the columns are ordered so that their distance from the diagonal is roughly proportional to their distance from the pixel itself. The second row of bands visible at the top and bottom (which differ from the previous figure) indicate that this approach yields noise with some cyclicity to it, rather than just a simple monotonic decay of correlation vs. distance. This is likely more similar to real data. The figure to the right is the covariance structure for a single data point shows the decay of correlation with distance for a pixel in the center of the image.

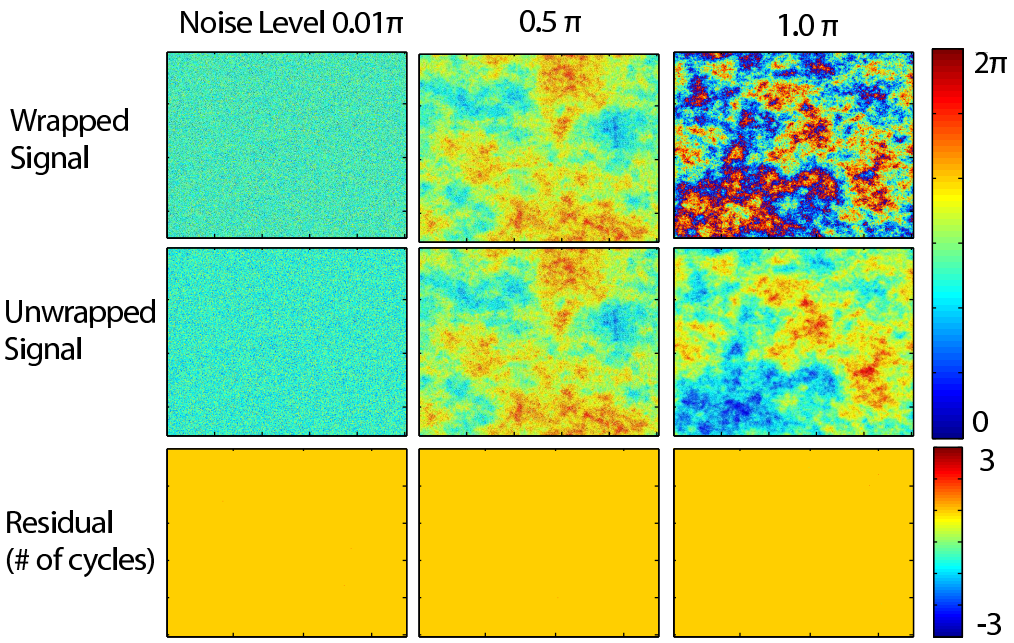

Figure 2.14: Unwrapping results for different levels of atmospheric noise. The top row is the input signal after wrapping. It is unwrapped using Snaphu (middle). The residuals for each noise level are shown in the bottom three row all are zero.

smooth and the phase variation from pixel to pixel is low, the cross-correlation constant stays near 1.0 for all cases, which shows that Snaphu handles spatially smooth signals very well if decorrelation (i.e., the white noise component) is low.

2.5.3 Spatially Correlated Noise+Ramp

Interferograms often contain linear or quadratic phase gradients across the entire image, caused by the inaccuracy of estimated satellite orbits, long-wavelength variations in atmospheric water vapor, or even the desired, tectonic signal; here we call this feature the ramp. Since the ramps add complexity to the

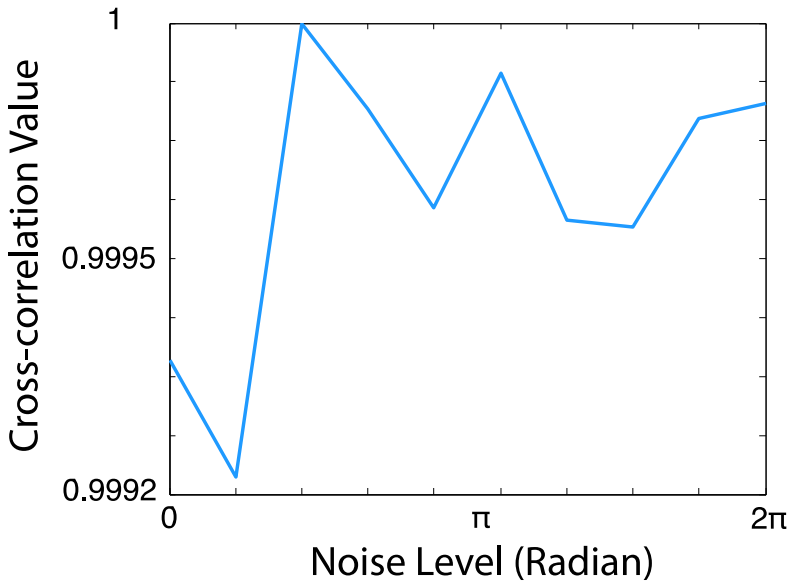

Figure 2.15: Normalized Cross-correlation. The correlation values are the average of 20 runs with different set of noise. The values remain high, for correlated noise at all noise levels between 0 and 2π.

interferogram, they have the potential to further degrade the unwrapping solutions. In the following, I examine the effect of ramps including different level of correlated noise on the fit of the unwrapped result to the true solution.

The cross-correlation values only differ slightly (< 0.1%) as it is shown in Figure 2.16; therefore, the effects of the orbital ramp is not significant to our unwrapping result in the case where everything else is the same within the image. This is not surprising, since a ramp is similar to spatially correlated noise with a long spatial scale. However, as we will see in the next section, ramps can introduce difficulties when there are gaps in correlation within the interferogram.

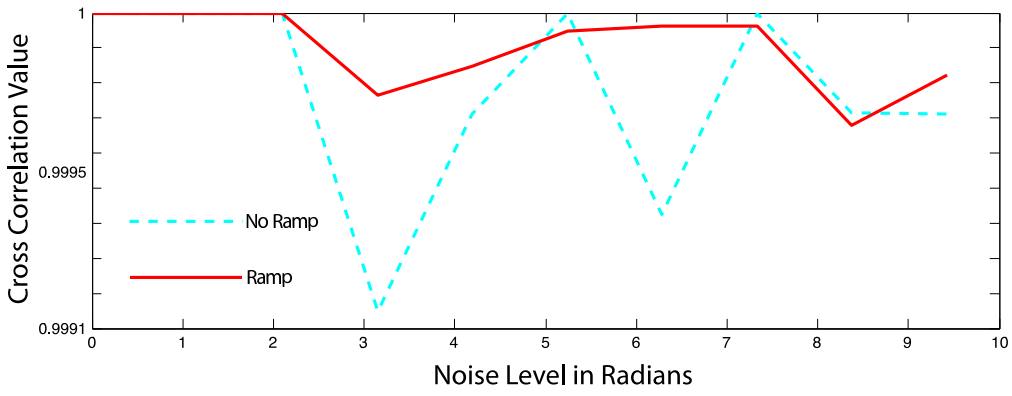

Figure 2.16: Normalized cross-correlation for data with and without ramp. Addition of ramp does not significantly improve nor degrade our results. The cross-correlation values here for each data point are each an average of 20 different runs.

2.6 Imperial Valley Case: Unwrapping Realistic Signals with Decorrelated Regions

Previously, we showed with our synthetic tests that Snaphu is able to produce robust unwrapping results if the level of noise is below a certain level, particularly if the noise has some spatial correlation that results in low phase gradients. In our tests, decorrelation was represented by the level of white noise and was constant across the whole region. As soon as the white noise present in the input signal was sufficiently large, the wrapped signal would contain apparently random jumps in phase between all adjacent pixels and the data would be completely decorrelated. In the real world, almost all interferograms consist of correlated areas as well as numbers of distinct decorrelated regions. These decorrelated regions can become major sources of unwrapping errors, particularly when decorrelation is extensive, as we find in the Imperial Valley case. In the Imperial Valley, extensive agriculture activities and water bodies such as

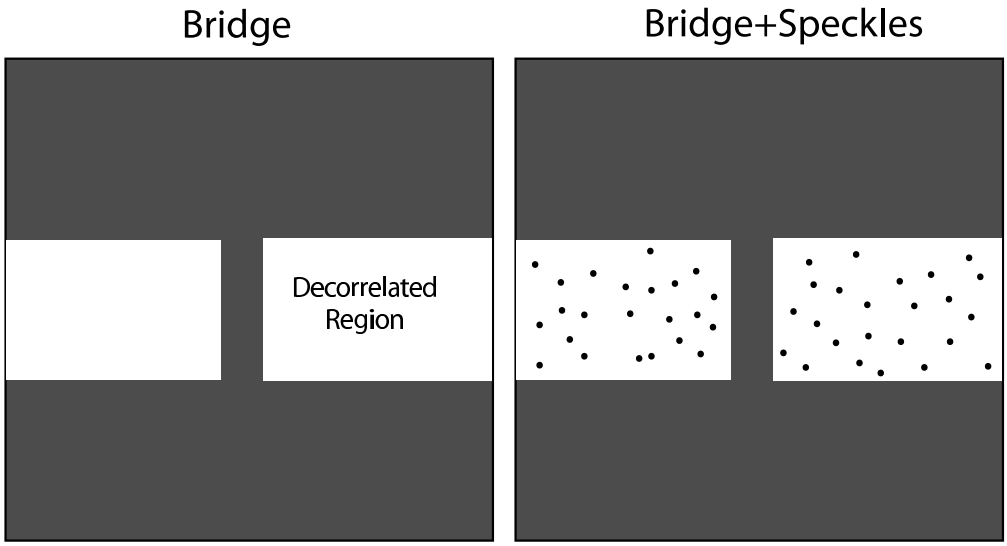

Figure 2.17: Imperial Valley scenario, including decorrelated regions (white). (Left) Inclusion of a bridge connecting the two correlated regions (gray) to improves unwrapping, representing a freeway or other major road. (Right) Isolated coherent pixels within the decorrelated regions, representing cities and other stable ground targets.

the Salton Sea result in decorrelation within the center of most interferograms. However, we observe many existing coherent features (roads and cities, for example) within the central problematic region that can be utilized to improve the unwrapped solutions.

To test this approach, I create synthetic interferograms that simulate the Imperial Valley environment. The center of each synthetic interferogram is masked out as if it were completely decorrelated (Figure 2.17). I add a narrow bridge connecting both sides of the image to simulate the presence of coherent, man-made features such as roads, as well as randomly distributed, coherent pixels representing cities and stationary ground targets such as buildings and parking lots. Figure 2.17 illustrates the two different test cases I will demonstrate later.

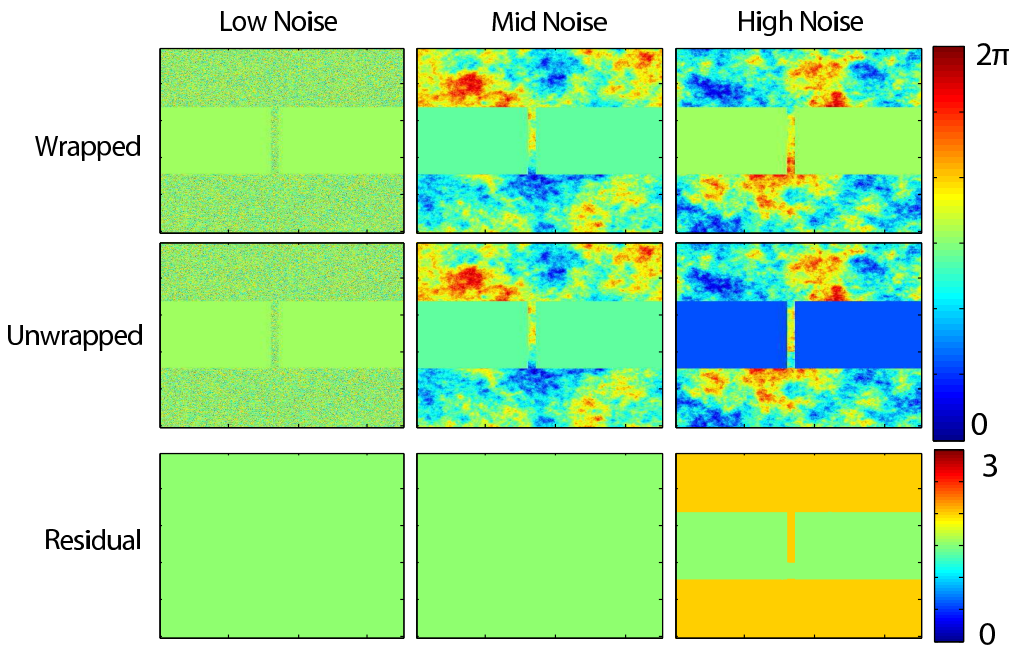

Figure 2.18: The effect of unwrapping with addition of a bridge connecting two sides of coherent area. Our testing results show that Snaphu is able to provide a good solution for all cases shown here, despite having some slight unwrapping errors at high noise

2.6.1 Regions with Connecting Bridge: Correlated noise

Here I create the same types of signals that we used in the section on spatially correlated atmospheric noise, masked as shown in Figure 2.17. In Figure 2.18, white noise level is kept low and I vary the magnitude of atmospheric delay, lowest in the left most figure and highest in the right most figure. The noticeable unwrapping errors begin to emerge as the atmospheric signal magnitude exceeds half a cycle.

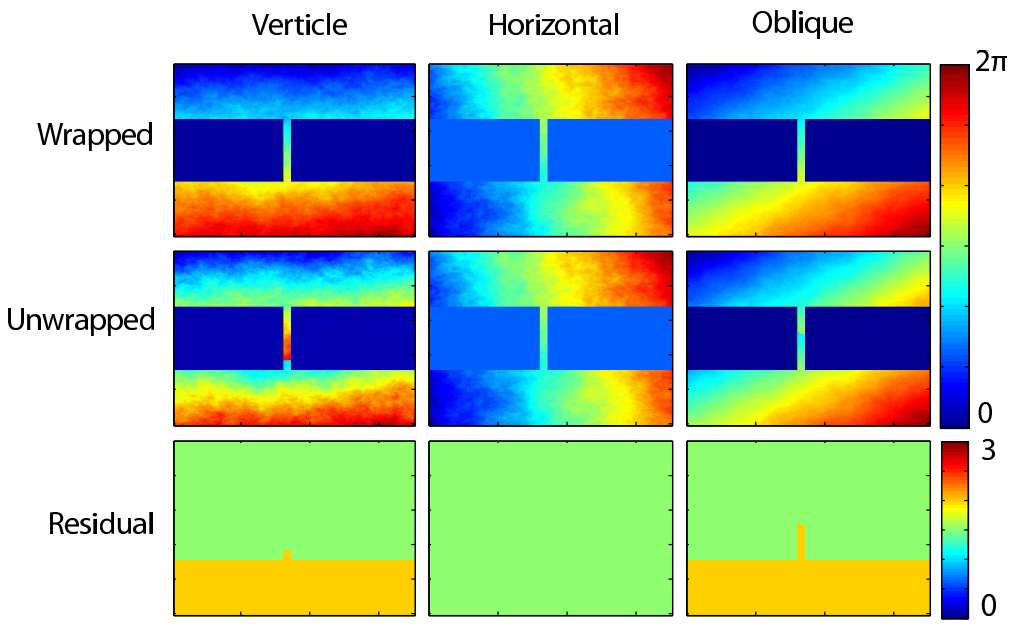

Figure 2.19: Ramp degrades unwrapping results when two coherent areas are only connected by a thin bridge. Here we test the effect of different ramp orientations on the unwrapping result. The result is best when the ramp gradient is perpendicular to the gap (or vertical to the bridge).

2.6.2 Regions with Connecting Bridge: Effect of Ramp

The effect of gaps in data are exacerbated when there are gradients in the noise or signal that are parallel to the gap itself it becomes difficult to determine how many cycles must be added or subtracted across the gap. The effects on phase unwrapping using different phase ramp orientations are examined here. In refer to Figures below, we examine the ramps that are perpendicular, parallel, and oblique to the decorrelation gap. Like the previous tests, I keep the white noise level low, and atmospheric delay signal level slightly below π.

Notice that the unwrapping results vary with ramp orientation. As it is shown in above figure, the unwrapping residual in Figure 2.19 between both

sides of the synthetic interferogram is off by a cycle when the ramp gradient is parallel to the gap. This is to be expected if the shift in cycles between two *equi-cycle* surfaces occurs in a region with little data, e.g., the gap between the two sides of the valley, then the unwrapped solution will be more poorly constrained than if the ramp is perpendicular to the gap and the phase values along the narrow road crossing the gap do not contain any 2π jumps.

2.6.3 Speckles

Stationary ground targets such as cities and parking lots often remain coherent and can potentially be utilized to improve unwrapping if their density is sufficiently high. We create synthetic tests to examine the robustness of Snaphu unwrapping in the presence of these speckles, which can be identified using a variety of approaches including both magnitude and phase stability (*Ferretti et al.* (2001), *Hooper et al.* (2004)). In a similar fashion as in to the previous section, we mask out the rest of the decorrelated gap region, and unwrap the data before comparing it to the true solution (Figure 2.17). We first test the effect of level of spatially correlated atmospheric noise. Figure 2.18 demonstrates that varying the atmospheric signal level does not affect the unwrapping results significantly. As we vary the density of speckles from low to high, the unwrapping errors begin to disappear beyond 40% of density (Figure 2.20). The cross-correlation value also increases, as we increase the density. Applications of this testing approach to real data would require consideration of how the real density of good scatterers within the valley compared with the scales of spatial correlation in the noise within individual interferograms.

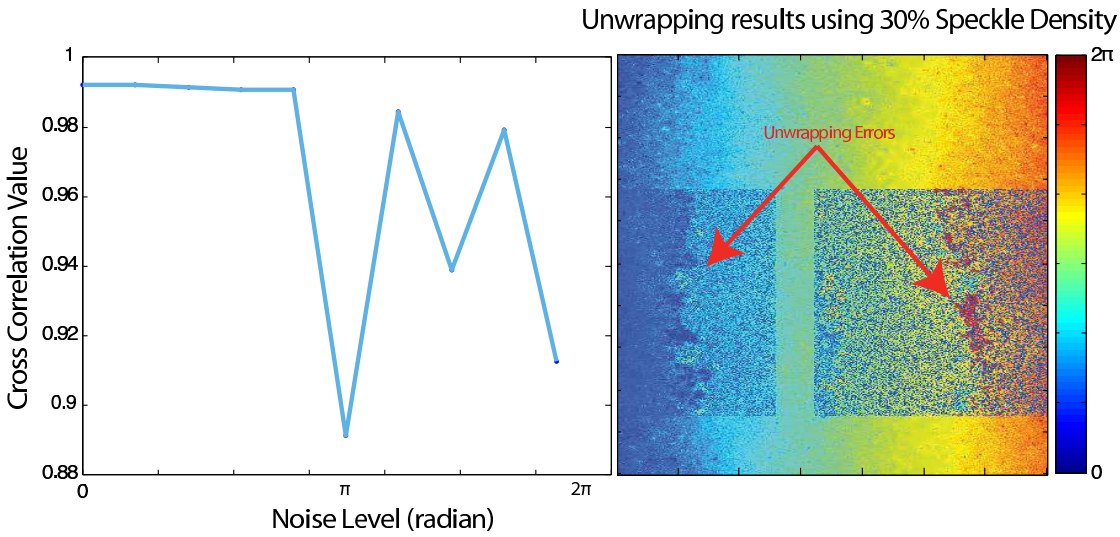

Figure 2.20: Varying the level of atmospheric noise does not have strong effects on unwrapping results. The cross-correlation values are averages of 20 different runs. The figure to the right shows the actual unwrapping results using a density of coherent targets within the decorrelated zones of 30%, unwrapping results are indicated by the arrows. As it is shown on the graph, the different noise levels explored here do not result in large changes to the cross-correlation values.

2.7 Summary

We test the robustness of Snaphu unwrapping algorithm under several scenarios. We have demonstrated Snaphu is very robust if coherency is high and noise level is low (realistically, white noise is very low). However, unwrapping errors can be introduced when large decorrelated areas exist and spatially correlated noise level is high. The effects of isolated regions of coherence is also demonstrated in our "speckle" tests (Figure 2.21), showing that , that clear unwrapping errors emerge as the density of coherent points drop below 70%. This effect is likely to depend on the spatial scale of the correlated noise - noise correlated over larger scales will require less dense sampling than noise that is correlated

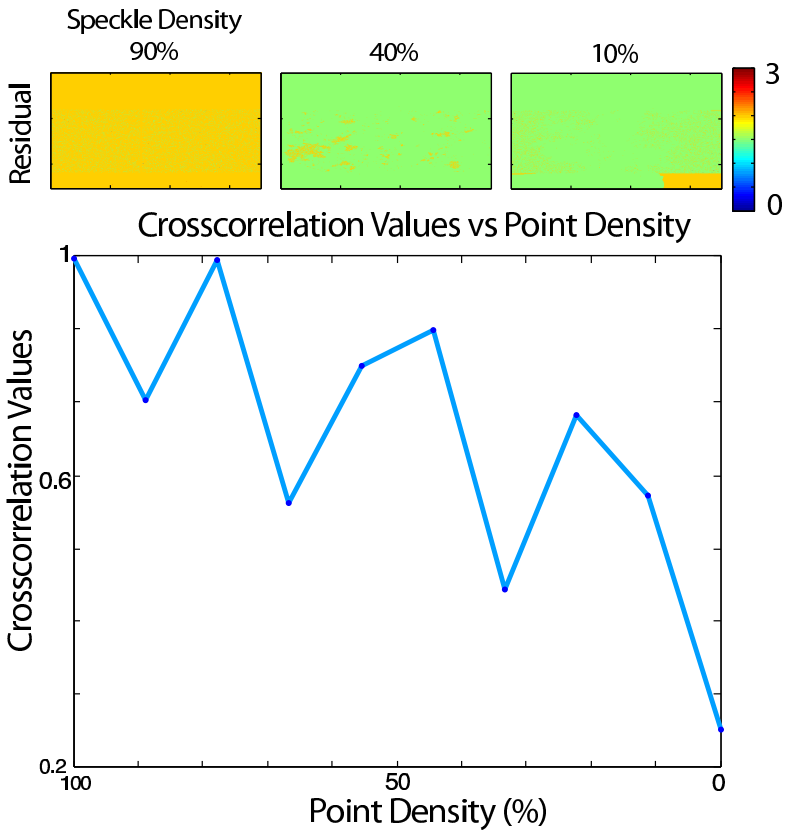

Figure 2.21: Variations in density of coherent scatterers: Higher density of data points in the decorrelated region results in good unwrapping results, whereas, sparse data points cannot be unwrapped well, as we expected.

over shorter spatial scales.

CHAPTER 3

SOME INSIGHTS INTO SLIP INVERSIONS

3.1 Introduction

Traditional geodetic techniques such as campaign Global Positioning System (GPS) surveys and leveling can have very limited spatial resolution since each individual measurement requires a significant amount of manpower. Continuous-mode GPS reduces the amount of field time required for each measurement, but comes at a significant cost (10s of thousands of dollars) for each new site. Repeat-pass Interferometric Synthetic Aperture Radar (InSAR) provides dense deformation measurement over areas of around 100x100km or more, making this geodetic technique a very powerful tool for retrieving the deformation field (at least, the portion of it not underwater), and thus greatly improves our knowledge of deformation associated with the earthquake rupture process. The dense spatial coverage (~20 meter pixels) provided by InSAR places strong constraints on rupture characteristics on a fault zone since small deformation features associated with fault stopovers and along-track variations in slip can be captured and used to constrain rupture behaviors. The primary motivation of this chapter is to examine the resolution that InSAR can place on shallow fault-zone properties. I will describe how rupture or interseismic slip characteristics can be derived from geodetic data and the robustness of the solution from the given data.

Typically, obtaining rupture characteristics of a fault based on geodetic data, such as InSAR, involves solving two optimization problems. The first is to search for the best fitting geometry of the fault, and the second is to infer a

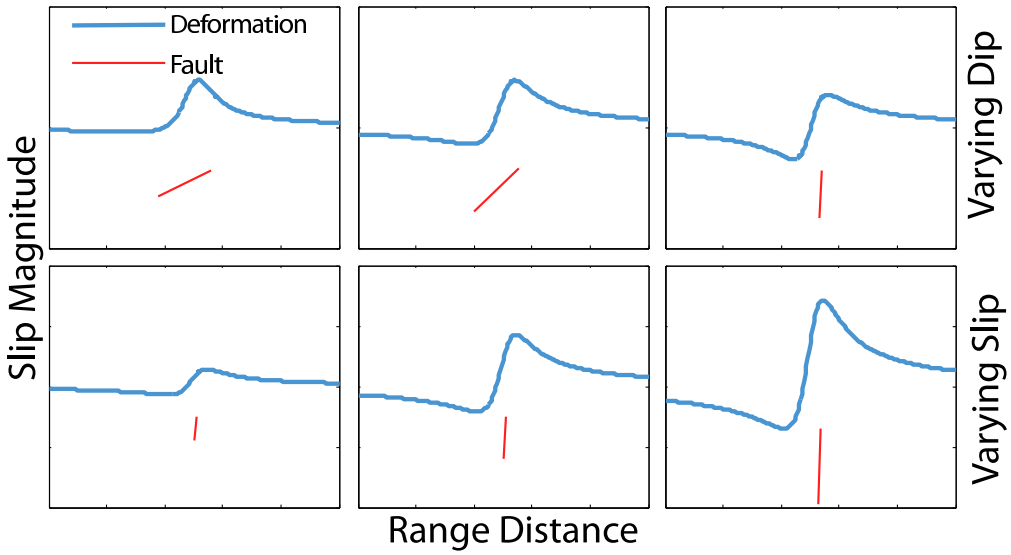

Figure 3.1: Effect of varying geometry and slip on the deformation pattern. Top row: Varying dip changes the overall shape of the deformation pattern. Bottom row: Varying the slip results in no change in deformation shape, only a change in the magnitude.

slip distribution on that particular fault parameterization. Estimating the best fitting fault geometry is a nonlinear problem since the shape of the predicted deformation for a given geometry varies significantly depending on the strike, dip and rake, as well as on the location and depth (Figure 3.1).

Estimating the slip distribution is a linear problem Figure above when no other constraints are added (such as requiring that slip be right-lateral) and can be solved using standard least-squares approaches. Only a small section in this thesis is dedicated to the conventional geodetic slip inversion problem since the technique is very well documented in the literature (e.g., *Segall and Harris* (1987), *Du et al.* (1992), *Jonsson et al.* (2002)). My primary interest here is to further explore the methodology and ultimately provide an assessment of the robustness of the inversion results. Eventually, we want to assess the constraints that avail-

able InSAR data can place on the Imperial Fault, since the Imperial Valley is a very challenging place for InSAR, with extensive decorrelation from agriculture and atmospheric artifacts due to large water vapor contrasts between the desert and Gulf of California. The tectonic deformation signal that we are seeking to model may also be contaminated by anthropogenic and seasonal effects.

The goals of an inversion of geodetic data for fault zone behaviors include accurately constraining the deformation, understanding the error bounds associated with that deformation, and assessing the model resolution that our data is able to provide. Eventually I wish to use geodetic data to further constrain the geometry and slip behavior of the Imperial Fault in southern California; however, here I explore the initial step of examining several theoretical scenarios that are similar to the real-world problem in the Imperial Valley. The actual work using InSAR to study deformation in the Imperial Valley may be conducted in the future. In this chapter, I will discuss several approaches that I used during the inversion. I first review the basics of inverse problems, data sampling, and model regularization related issues. I then discuss the sensitivity of these inversions using our synthetic test results.

3.2 Slip Inversion: Setting up the Problem

Surface deformation associated with motion along faults is often modeled using a model of a dislocation within an elastic half space (e.g., *Segall and Harris* (1987)). For more complex deformation fields that reflect a spatial variation in the amount of fault slip, researchers often invoke a complicated fault plane made up of many dislocations, or fault patches. Our general assumption here

is: The net surface deformation is the sum of the contribution from slip along every dislocation patch within the elastic material making up the Earth subsurface. The contribution of the surface deformation from every dislocation patch can be computed using an existing analytical solution for dislocations within an elastic half-space (*Okada* (1985)). Figure 3.2 shows how surface deformation is predicted based on a given dislocation plane with a known subsurface slip distribution. This prediction, where the physics relating observations to quantities such as subsurface fault slip are known, is referred to as the forward problem.

Our goal here is to obtain a slip distribution from a given set of surface deformation data. This can be treated as a linear problem of slip on a known fault plane in a material with known elastic properties. This may not necessarily be an accurate approximation due to the fact that earthquake ruptures are complicated and dynamic, and occur in a heterogeneous material with many unknown planes of weakness and material contrasts. We also do not account for any anelastic responses of the material and variations from our model of the fault plane geometry; however, the elastic half space assumption simplifies the problems significantly and estimates of the contribution from several known sources of heterogeneity predict variations in inferred slip on the order of around 10% (e.g., *Masterlark et al.* (2001)).

We can express the linear problem where the surface deformation is the sum of the contribution from the slip on all patches at depth with the following equation:

$$d_{obs} = Gm_{true} + e \tag{3.1}$$

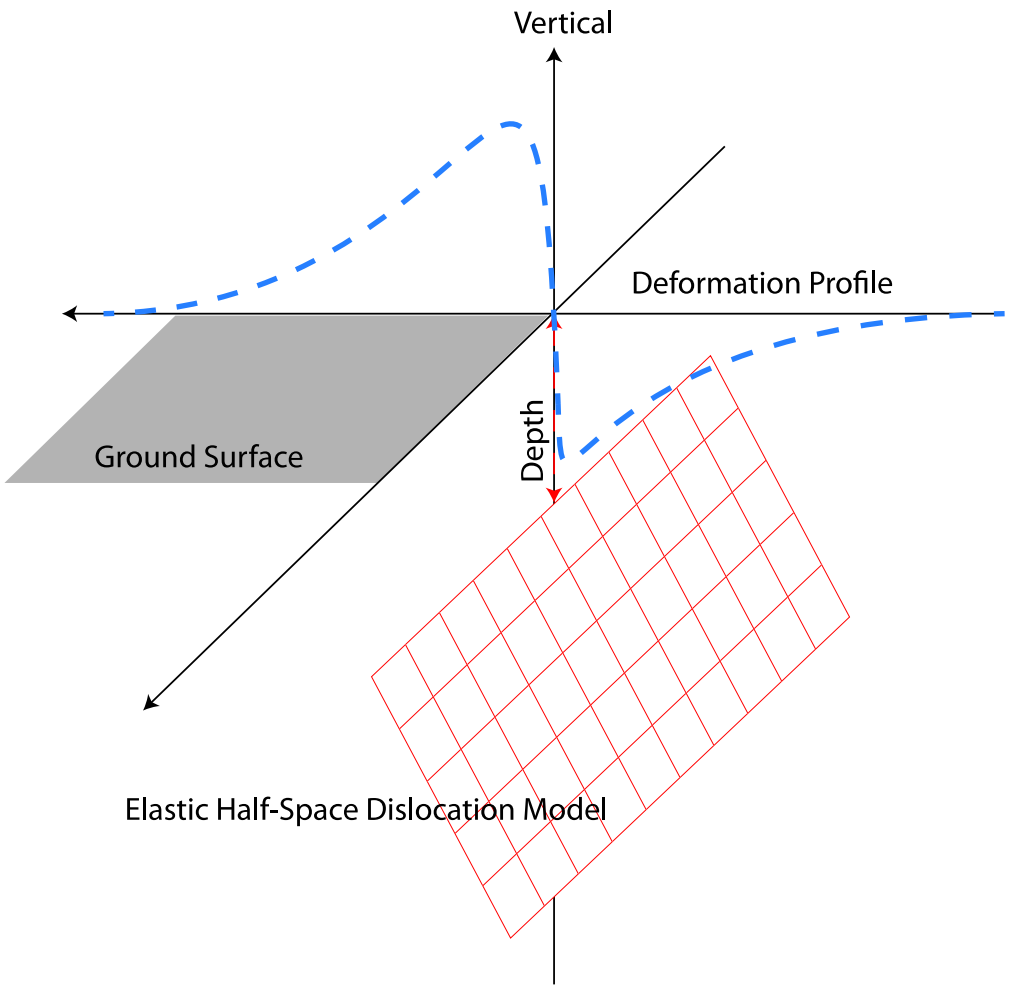

Figure 3.2: Elastic half-space dislocation model. The orange inclined plane is the fault, discretized into a number of fault patches. The blue dashed line on the surface is the inferred deformation due to slip on the fault plane.

d_{obs} is the observed displacement, G is the linear response function for slip on a dislocation embedded in an elastic half space (a.k.a our Greens function), m is the slip distribution, and e is the error within the data observations themselves. In practice, there will also be errors due to non-tectonic sources of ground deformation such as the extraction of groundwater or subsurface hydrocarbons, as well as any errors in our characterization of the fault plane geometry and

subsurface elastic properties. For inverse problems, we want to find the best fitting model, m, explaining our observations, d_{obs}. In other word, we want to find the best fitting parameters that minimize the prediction error, $d_{obs}\ \ Gm$. In general we quantify the prediction error by taking the L-p norm of the misfit between the observation and prediction. Here, in Equation 3.2 d_{prd} is the data predicted using a model, m_{est}, and R_{pen} is the penalty such that a poor fit to the data receives a large value and a good fit is associated with a small value.

$$d_{prd} = Gm_{est} \tag{3.2}$$

$$R_{pen} = |d_{obs} - d_{prd}|^p \tag{3.3}$$

The right half of Equation 3.3 is the L-p norm of the misfit between observation and prediction. The penalty value R_{pen} also depends on the value, p, ranging from 0 to infinity. Different p values may vary the inversion results quite significantly; typically the L-2 norm (the least-squares norm) is used for most parameter fitting problems since a convenient matrix solution can be easily derived. In the following section, I describe the most commonly used inversion technique, the least-squares solution.

3.3 Slip Inversion : Weighted Least-Squares Formulation

The least-squares solution is obtained by minimizing the derivative of the L-2 norm formulation described above with respect to the parameter vector m. In matrix form, the solution to this minimization is shown in Equation 3.4 with a derivation described in *Menke* (1989)

$$m_{est} = (G^T G)^{-1} G^T d \tag{3.4}$$

Here, the vector m contains the estimated model parameters, d is the data vector, and G is the response kernel that relates the model to our data. Equation 3.4 is only uniquely solvable if $G^T G$ is invertible. The first requirement for $G^T G$ to be invertible is that the data vector is longer than the model vector, i.e., that we have more data than unknowns, also known as having an overdetermined problem. However, as we will see below, we often still run into issues with least squares inversions even when we nominally are dealing with an overdetermined problem. $(G^T G)^{-1} G^T$ is often referred to as the generalized inverse (*Hansen* (1987)), and is generally denoted as G^{-g}, from which we can make some very useful inferences about our data/model resolution. If the error associated with the data varies from point to point, we can apply different weights, W, to the error (Equation 3.3), and the (Equation 3.2) can be expressed in the following way:

$$R_{pen} = W \| G m_{est} - d \|^2 \tag{3.5}$$

$$m_{est} = (G^T W G)^{-1} G^T W d \tag{3.6}$$

This formulation results in a model that depends most highly on the data points that have the best constraints. One of the most important issues with inverse problems is the determination of whether the solution is realistic or not. The inversion only provides the best fitting solution to the data, regardless of the realness of the solution. In other words, the inversion attempts to fit the actual signal caused by physical changes within the earth, as well as any noise

in the signal. Even in cases where we nominally have more data points than unknowns, the information content of those data points may be highly correlated, leading to a mixed-determined scenario. Therefore, we must often attempt to limit the set of solutions to the inverse problem to those that are realistic in some sense, a process referred to as regularization. This typically involves approaches that constrain some characteristic of the solution, such as those that require that the solution be spatially smooth or have limited size by some measure. In section 3.4, I will discuss regularization in detail.

3.3.1 Singular Value Decomposition

Singular Value Decomposition (SVD) is another approach to invert for the best fitting parameters, and shares many qualities with least-squares approaches. The SVD approach decomposes a matrix into linearly independent row and column bases, and corresponding singular values in the following way:

$$G = U\Sigma V^T \tag{3.7}$$

In slip inversion problems, the matrix G usually has size ixj, where i is the number of data points and j is the number of fault patches. The inversion algorithm using SVD can be expressed in the following format:

$$m_{est} = V\Sigma U^T d \tag{3.8}$$

Here, matrix U is an ixi unitary matrix, the columns of which are the data space basis. Matrix V is jxj unitary matrix, and the row of which are the model

space basis. Σ is a diagonal, ixj matrix, each diagonal entry contains singular values for the corresponding row and column basis.

The SVD approach describes how the data space (the row bases matrix U) is mapped into the different model parameters (the column bases V), scaled by singular values, the matrix Σ. The magnitude of the singular values indicates to the level of contributions of the corresponding parameters in an inverse problem. For example, if the problem is underdetermined (more unknown parameters than observations), the solution will be completely non-unique and therefore some portions of the model space will correspond singular values of zero. In other words one could add any combination of these parts of the model space (also referred to as the null space) to the solution and not change the predicted data at all. The conventional way to solve the problem is to truncate the very small or zero-valued singular values to maintain the stability of solution (this is also called solution damping). This can give exactly the same solution as the minimum length constraints described below.

3.4 Regularization

As previously stated, we often need to place constraints on our inversion to make our solution realistic. One approach to this is smoothing, where we limit the solution roughness, caused by unrealistic oscillations resulting from overfitting of the noise. Another widely used regularization technique for ill-posed problems is Tikhonov regularization. Tikhonov regularization constrains the norm of solution size, which has the side benefit of reducing model roughness. Tikhonov regularization is often referred to as the minimum length solution

(Equation 3.9):

$$min||Gm - d|| + \lambda||m|| \tag{3.9}$$

The first term in Equation 3.9 is the standard least-squares formulation with no added regularization and the second term is the penalty term, in this case related to solution size. The second term has the effect of adding pseudo-data to the inversion, bringing it closer to being overdetermined. λ balances the model penalty against the importance of misfit to the data. Small values of λ result in a good fit to the data with potentially large fluctuations in model values, whereas larger values increase the contribution of the penalty term and result in solutions that may be more realistic, but that do not fit the data as well. The graphical representation of such a relationship is commonly referred to the L-curve, with one axis showing the model penalty term (solution length, here) and the other axis showing data fit. The corner point on the L-curve, is typically selected as the optimal model that balances data fit and model characteristics. Note that in this example, there is a point where the data fit does not continue to worsen even as the model length continues to decrease (lower left in curve). This is due to the fact that, at some large value of λ, the model is near-zero and the data residual is equivalent to the data itself.

The effect of regularization can be illustrated in the example . Here I generate synthetic displacement data using a known dislocation model, and add spatially correlated noise. I then invert the data using a range of regularization values. Figure 3.3 is the L-curve associated with this example. In Figure 3.3, the bottom-left figure is the inferred model without any regularization, the bottom-right figure is the over-smoothed model, and next one is the optimally smooth

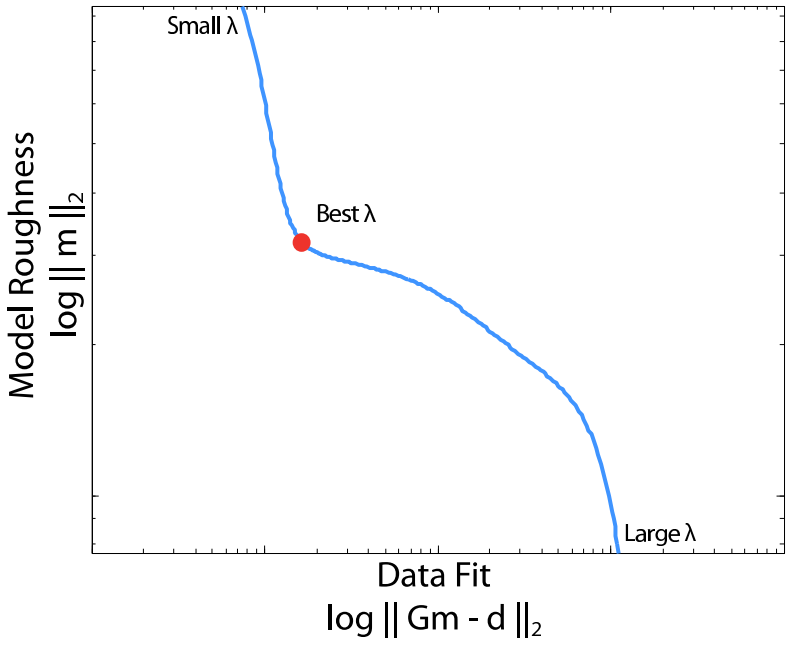

Figure 3.3: Log plot of model roughness vs data fit for different smoothing. When little smoothing is applied, we have the best data fit (smallest $\|Gm-d\|^2$), when large smoothing (large λ) is used, our estimated model is smoothest (lowest model roughness, $\|m\|^2$). Best smoothing is picked at the red dot, which is the corner of the L-curve.

model. Notice in Figure 3.3, the model size decreases as we increase the regularization. For the case of the non-smoothed model, the solution has the smallest least-squares residual; the inferred model however, exhibits unrealistic oscillations. The over-smoothed scenario exhibits a very smooth solution but has a large least-squares residual. Ideally, the optimal choice of regularization weight results in a data residual that is consistent with the characteristics of data noise, i.e., the noise is not being over-fit but the overall signal is not being under-fit. In Figure 3.4, I demonstrate small smoothing results in having the best data fit but unrealistic slip model, whereas optimum smoothing results in worse data fit but produces the more realistic slip model.

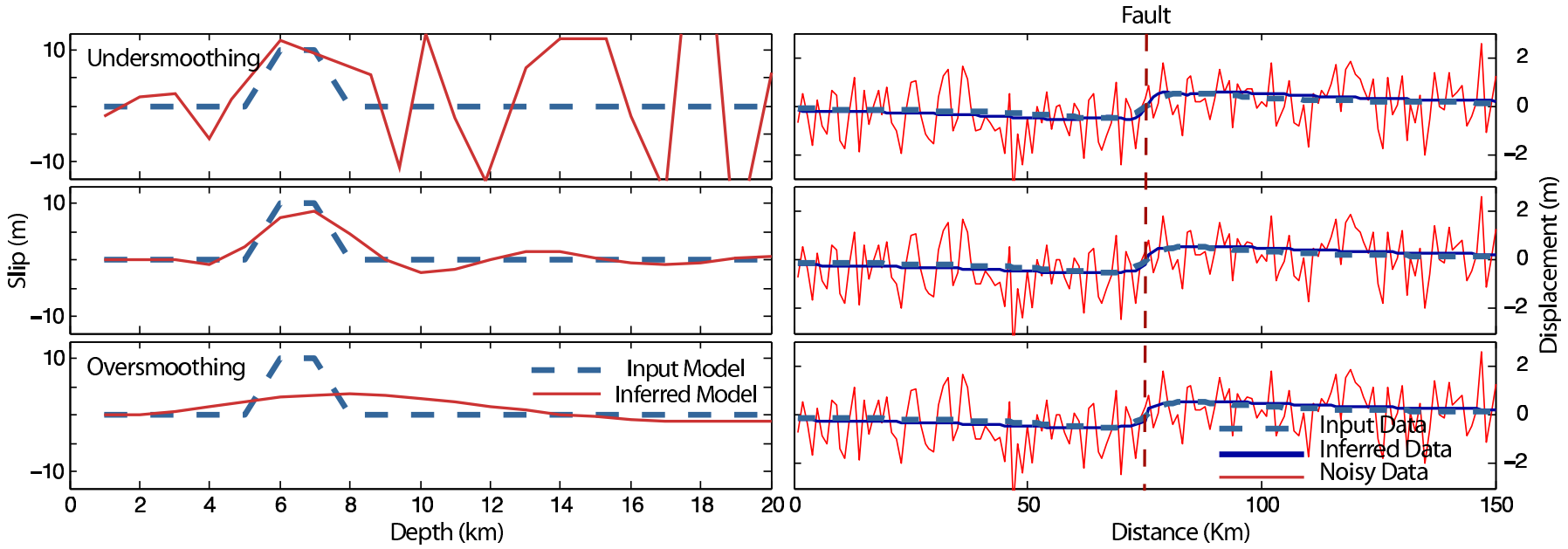

Figure 3.4: The effect of smoothing. For under-smoothing case (small λ), the solution exhibit strong oscillations and have the best data fit (residual root-mean-square (rms) = 11.67), for ideal smoothing (l-curve), rms = 11.9, and for over-smoothing case (large λ), the solution shows little spatial variability and have to worst data fit (rms=12.16). The residual here is calculated using the difference between the inferred data and noisy data.

An alternative way to select the ideal regularization value is through the automated *jRi* method (*Barnhart and Lohman* (2010), *Lohman* (2004)). This approach assumes that if the data noise structure is known, we can then search for the best regularization value that sufficiently penalizes the noise yet adequately fits the data. In the following figure, the curve shows the effect of regularization to noise and data fitting. Here, the data fitting error refers to the regularization error and noise-fitting error is the perturbation error (*Hansen* (1987)). The ideal regularization is such that neither term overwhelms the other we do not wish to overly fit the data nor over smooth the model.

3.5 Solution Uniqueness and Model Resolution

As previously discussed, linear inverse problems can be solved using the least-squares method using equation 3.6. The estimated solution can be written in the following form:

$$m_{est} = G^{-g} d_{obs} \tag{3.10}$$

where G^{-g} is some matrix that relates our data to the estimated parameters, in other words, the matrix G^{-g} maps our data to the model and is typically referred to the generalized inverse matrix. Regularization, as described above, can also be incorporated into the generalized inverse. Given a particular G^{-g} and its associated regularization, we can examine characteristics of our estimated model by defining a model resolution matrix R, in the following formulation:

$$m_{est0} = G^{-g} d_0 = G^{-g}(G m_{true}) = R m_{true} \tag{3.11}$$

here m_{est0} is the estimated model from a theoretical set of noise free data, d_0. The uniqueness of our estimated model can be determined by the structure of R, i.e., the closer R is, to identity matrix, the more uniquely determined our model is. With no regularization, R will be an identity matrix, and as regularization increases, each component of the model will become more and more of an average over a larger area of the fault plane. In summary, the choice of regularization weight, λ, is driven by the amount of noise in the data, and the character of R can aid in determinations of how spatially localized that output model is.

3.5.1 Resolution Test

As described above, inversions for the distribution of slip on a fault plane are not generally unique problems, and the trade-offs between different parameters can be large. For inversions of interseismic slip along the Imperial fault, for example, locking depth and slip magnitude strongly trade-off with each other. In general, dense data coverage near the fault zone allows both better spatial resolution and lower errors on inversions for fault slip, particularly in shallow portions of the fault plane. As part of the initial steps in the Imperial Fault study, we explore the dependence of achievable resolution for data sets with different noise and fault and rupture parameters by using a range of tests involving synthetic data.

In the following, I present my synthetic test results as the first step toward assessing our future slip distribution inversion results on the Imperial fault.

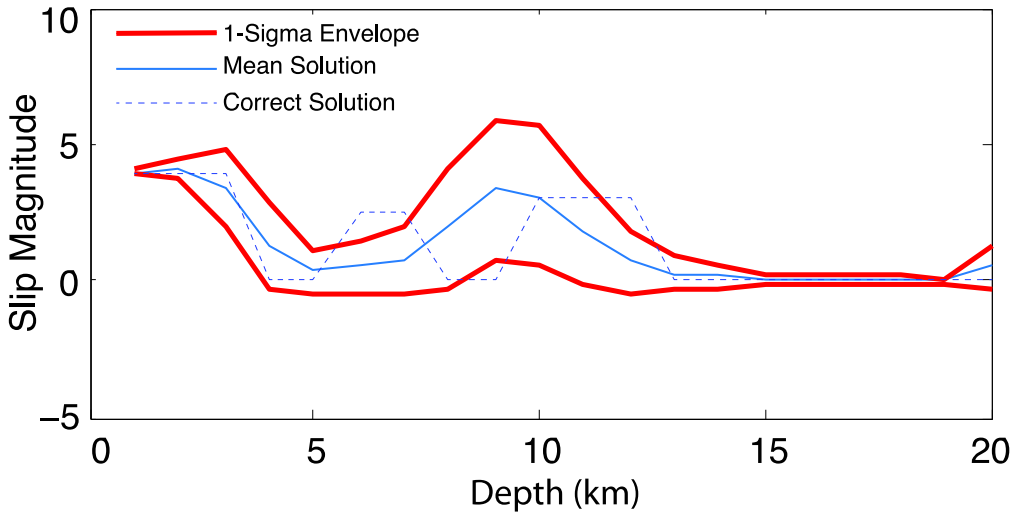

Figure 3.5: The original slip distribution error bounds is the dashed blue line, the best-fit inverted model is shown as the blue line, and 1 σ envelopes on fault slip are plotted as the red lines. Positivity constraints are imposed in this case.

We generate synthetic data from a known model, add many sets of noise with known characteristics, and then invert each of these independent noisy datasets for their best-fit solution. We then examine the mean and standard deviation (1 σ, ~68%) of the inferred models.

In this analysis, I use the vertical component of the deformation since the line-of-sight direction is mostly vertical. The fault is a vertical right-lateral strike slip fault with maximum depth of 25km and characteristics of slip, which I vary between the simulations. Our data is sampled on a 100km profile across the fault at spacing of 250m. We also added Gaussian white noise with variance of ~5cm, which is comparable to the noise level presented in real InSAR data.

In Figure 3.5, the thin blue curve is the input slip distribution, the red curve is the mean solution and the blue envelope contains candidate models within one standard deviation. The optimal smoothing here is picked using the jRi

method described above, which works very well when the characteristics of the noise are known and there are no additional sources of errors (such as the use of the incorrect fault plane, material properties, etc.). The mean solution is consistent with the input slip, as expected. As the data noise increases, this fit would worsen. To make the solution more realistic, I also constrain my slip distribution to be positive in Figure 3.5, since we might reasonably assume that we can tell whether a fault is right-lateral or left-lateral.

I explore the inversions sensitivity to locking depth by varying the depth range of slip used to generate my synthetic data. As is shown in reference to figure with varying locking depth, the inversion for slip becomes less sensitive (i.e., has a larger 1 σ envelope on the result), as we increase the slip depth for a given amount of slip and keep the noise constant. The effect is due to the fact that, as expected, the signal to noise ratio decreases as we increase the slip depth and move our source further away from the surface. Similarly, increasing slip magnitude also improves the constraints that the data places on the inferred model.

We are also interested in understanding the inversion resolution if multiple slip patches exist. Here I put two areas of slip at different depths, each having different magnitude of slip. I then vary the magnitude of slip for one of the patches, to examine the inversion results. Notice that, in reference to figure below our estimated solution uses a single patch to accommodate the slips on two adjacent patches as the slip magnitude of one patch becomes significantly larger than the other. As the separation between two slip patches increases the inversion is able to resolve shallow slip at higher magnitude, and put the deeper slip at greater depth with smaller magnitude.

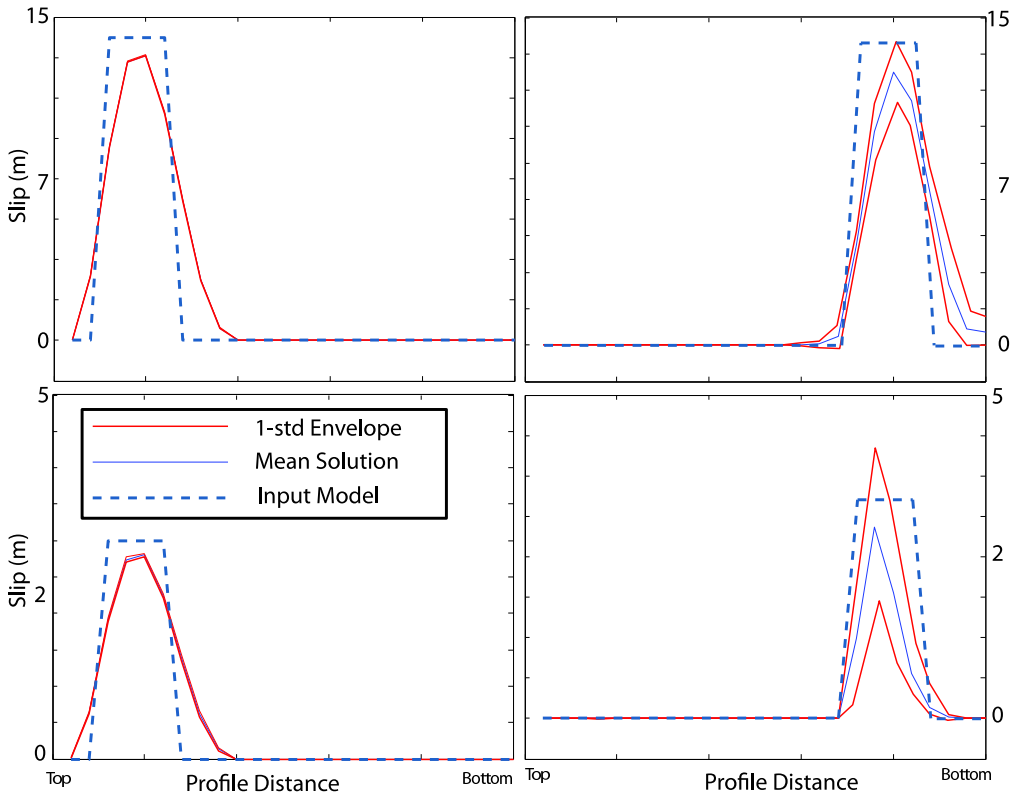

Figure 3.6: The figure shows the effect of varying depth to of peak slip with two different magnitudes. The resolution on shallower slip is always better than deeper slip. The solutions for larger magnitude slip (upper two figures) shows a narrower 1σ envelope than the solutions with smaller magnitude model (lower two figures) as expected, since the large slip results in a better signal to noise ratio.

3.6 Some Thoughts for the Future: Regularization and Vertical Slip Variation

The primary goal of this work was to understand the resolvable scale of slip heterogeneity on a fault plane using weighted least-squares inversions. In 2-D, I have shown that the magnitude contrast between adjacent slip patches (a significant large slip can shadow the adjacent small slip patch), depth of the

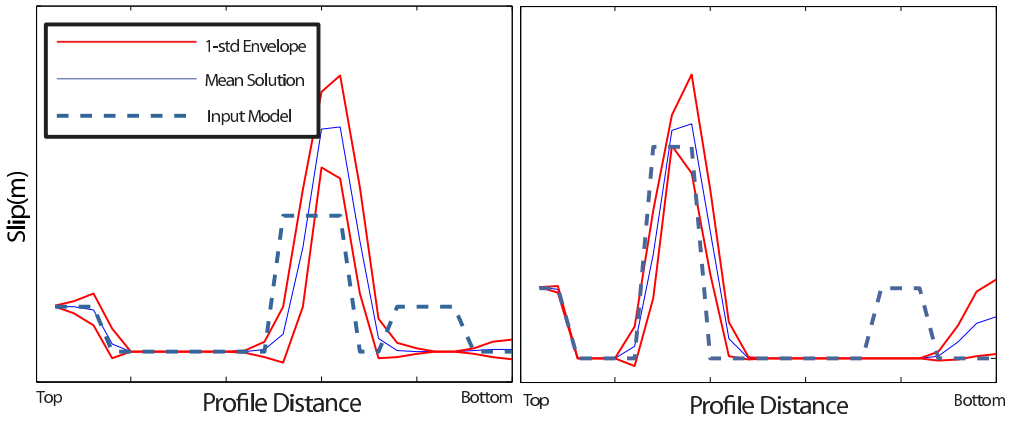

Figure 3.7: Inversions often merge the slip from two adjacent slip patches onto a single slipping region. As the two patches are more separated, the inversion becomes better at resolving both slip patches as distinct regions of slip. The resolution at depth however, is still poor.

dislocation, and resampling methods, all affect the ability of the inversion to resolve spatial variations in slip. The synthetic 2-D fault tests are also able to demonstrate the effects of different data coverages and sampling on the results. However, 2-D synthetic tests are not sufficient for us to fully understand the numerical characteristics of a 3-D fault. Ideally, we should be examining the sensitivity of our data to the varying strike, dip, rake, slip, and locations of the dislocation, as well as to variations in slip both along strike as well as down-dip. Since the geometry of the Imperial Fault is reasonably well constrained by geodesy and microseismicity, the locking depth and variations in slip distribution become our primary interests and the assumptions made here may be sufficient.

CHAPTER 4

INSAR OBSERVATIONS OF CRUSTAL DEFORMATION NEAR THE IMPERIAL VALLEY, CALIFORNIA : RESULTS AND CONCLUSIONS

I generate 48 interferograms from 38 ASAR acquisitions from the Envisat satellite deployed by European Space Agency, with short spatial (¡ 150m) and temporal (<1 year) baselines (Figure 4.1) using the JPL/Caltech developed ROI_PAC software (*Rosen et al.* (2000)). I diverge from some other time series approaches at the first stage where we create Single-Look Complex (SLC) images for each date that will then be used in interferogram generation. Ideally coregistration of a group of interferograms is optimized using a fixed Doppler centroid for all scenes; however, using the mean Doppler between each pair of images may result in better focusing in individual interferograms. Since our main problem is coherence, not image registration, we choose to generate our interferograms with the latter approach, by optimizing the Doppler centroid for each pair of images. The interferograms are made at full resolution. I then register, rectify, and remove the simulated effects of topography using the SRTM Digital Elevation Model (*Farr* (2000)) from all interferograms.

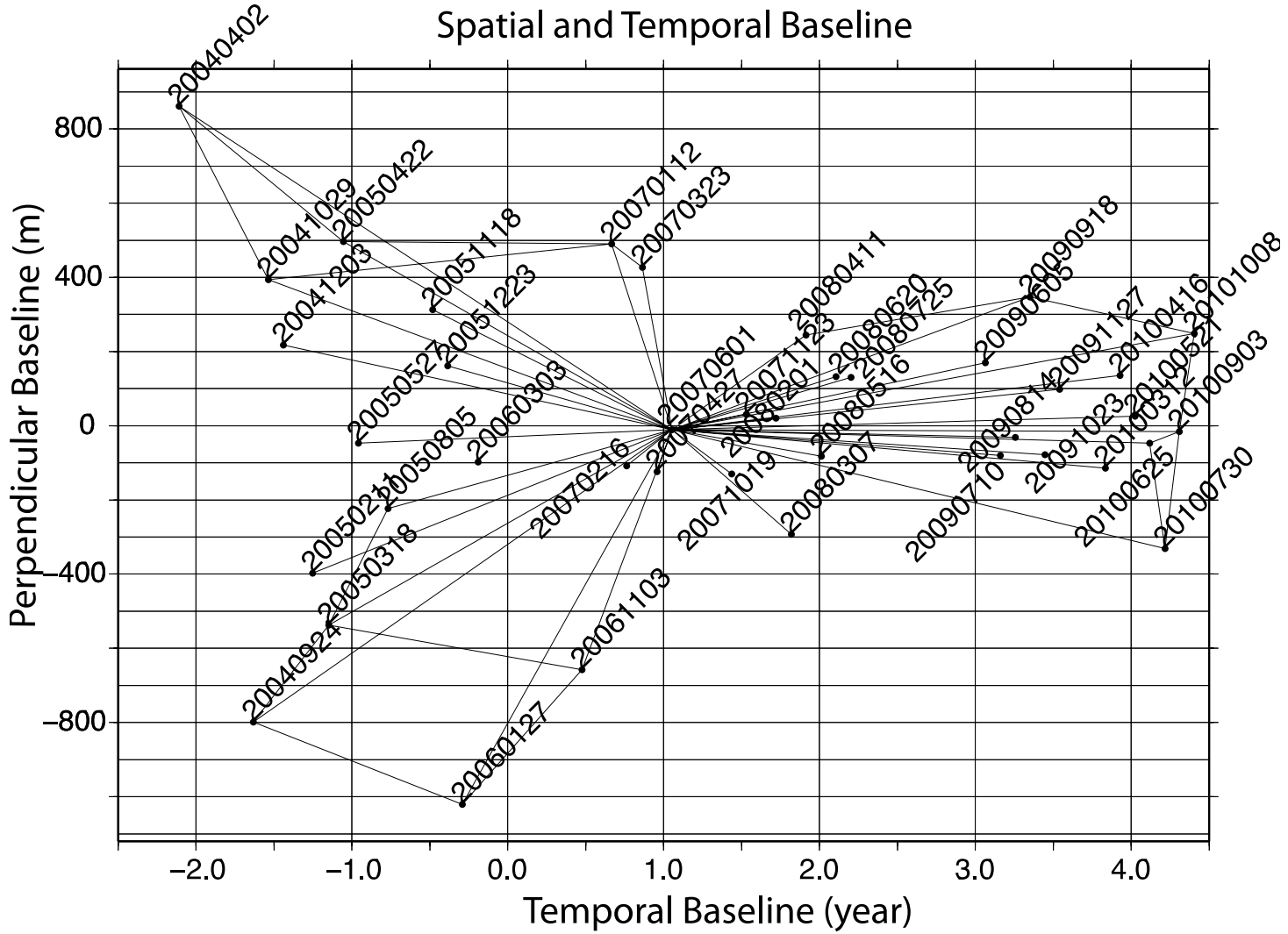

Figure 4.1: Our data plot in yyyymmdd format. Each dot represent a single acquisition with time and distance (temporal and spatial baseline) relative to a reference date and distance. Each line represent an interferogram constructed by an image pair.

The area suffers strong decorrelation due to presence of water bodies such as the Salton Sea, as well as from extensive agriculture activities. Therefore, we need to mask out the incoherent regions so that they do not contaminate the rest of our processing stream (Figure 4.2). We generate our mask by first cutting out pixels having correlation values below a certain, relatively low threshold (i.e., we still retain many points with poor correlation). We then improve the mask by running a moving window across the interferogram and only retaining points that tend to have phase values that are similar to the phase values of surrounding good points. This approach is based on *Hooper et al.* (2004) and requires several iterations to obtain a robust result. A good mask would be defined as one that masks out the water body and any fields that are not lying fallow throughout the timespan covered by our data. Remaining roads, cities and correlated areas are unmasked.

After masking, I average all interferogram to a lower resolution to improve phase noise, follow by phase unwrapping processing using Snaphu, to convert the interferogram phase measurements into actual deformation. I then use the Small Baseline Subset (SBAS) [*Berardino et al.* (2002)] method to extract the deformation time series during the data time span.

4.1 Methodology Small Baseline Subset Time Series Method

The Small Baseline Subset (SBAS) time series method has been widely used in the InSAR community to produce deformation time series (e.g. *Tizzani et al.* (2007), *Li et al.* (2009)). As it is described in Chapter 1, interferometry can be decorrelated by large spatial baselines due to geometric distortions, and large

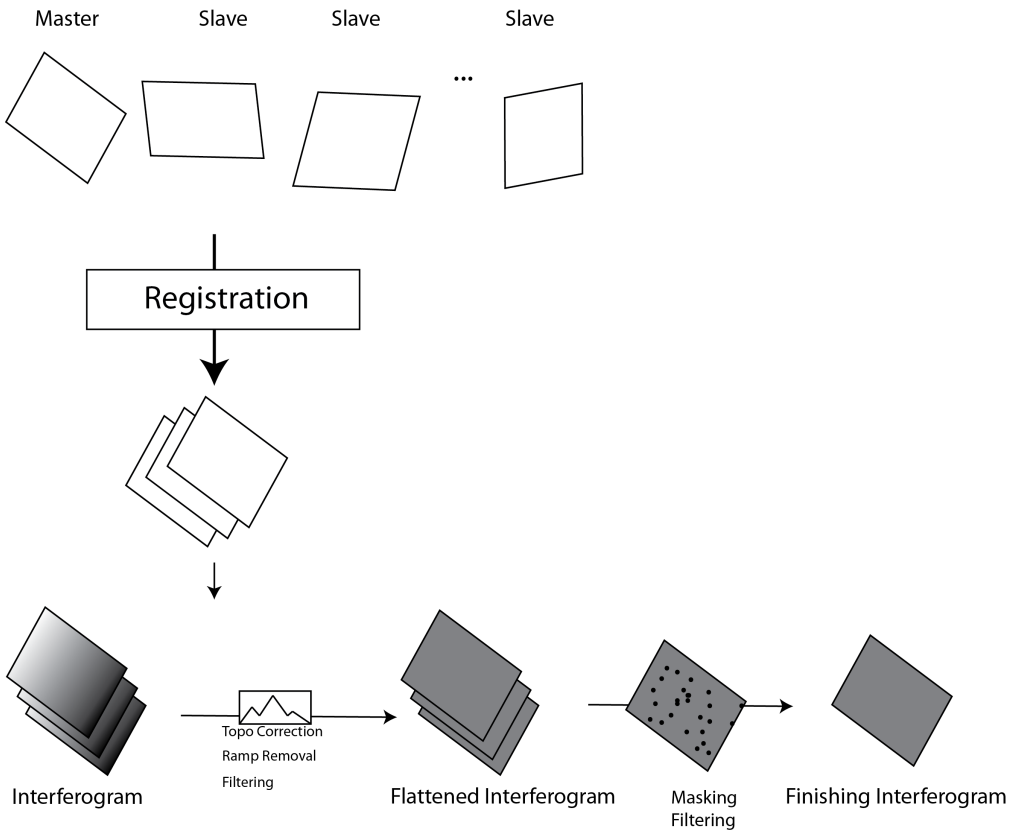

Figure 4.2: The figure shows our stepwise processes for forming and correcting an interferogram..

time separation in acquisition due to change in reflectivity of surface. The essence of the SBAS algorithm is that it uses a large network of small baseline interferograms that are optimized for maximum coherence to estimate the deformation time series. The set, or tree, of interferograms may include many redundant pairs that use particular dates again and again this approach minimizes the impact of unwrapping errors that may occur in individual interferograms. If many individual acquisitions are used to form this tree, atmospheric delay signals can potentially be cancelled out, or, at least, reduced.

The deformation time series is estimated for every pixel using singular value decomposition of the set of interferograms spanning a range of temporal and

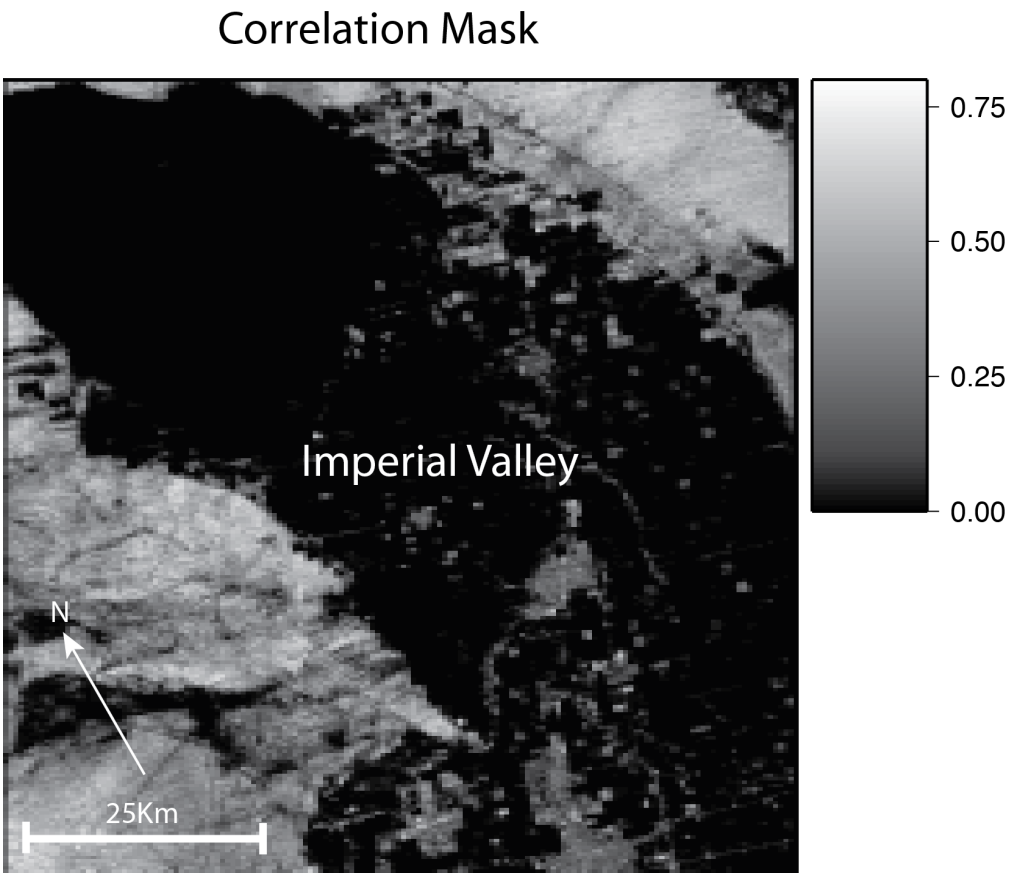

Figure 4.3: Our correlation mask. Darker pixels are poorly correlated; brighter pixels show higher correlation values. In the center of the Imperial Valley, most regions are poorly correlated, except some features such as cities and roads.

spatial baselines. The problem is formulated in such way that the cumulative deformation from the first acquisition is estimated for each subsequent date, as if one had formed all interferograms relative to the first date (which would likely have included many poor-quality interferograms).

In Figure 4.4, *dtn* represent the time span from time t_{n-1} to time t_n, *vn* is the deformation rate during the time interval from t_{n-1} to t_n. Each interferometric pair, l_n, is the summation of the rate in each interval spanned by the interferogram multiplied by that time span. We first invert for the rate at each time interval,

(1)

$$\begin{bmatrix} & dt2 & dt3 & & \\ dt1 & dt2 & dt3 & & \\ & & dt3 & dt4 & \\ & dt2 & dt3 & dt4 & dt5 \end{bmatrix} \begin{bmatrix} v1 \\ v2 \\ v3 \\ v4 \\ v5 \end{bmatrix} = \begin{bmatrix} I1 \\ I2 \\ I3 \\ I4 \\ I5 \end{bmatrix}$$

(2)

$$\begin{bmatrix} d1 & d2 & \dots & dn-1 & dn \end{bmatrix}^T = \begin{bmatrix} dt1 \\ dt2 \\ \dots \\ dtn \\ dtn-1 \end{bmatrix} \bullet \begin{bmatrix} v1 \\ v2 \\ v3 \\ v4 \\ v5 \end{bmatrix}$$

Figure 4.4: Two approaches for to estimating deformation velocity from a sequence of interferograms. Equation (1) give us the velocity for each time interval (2) gives us the total accumulated deformation at each acquisition relative to the first date.

than calculate the cumulative deformation using the second equation.

4.2 Results

Several deformation areas can be identified in our mean velocity map (Figure 4.5). Of particular interest are the deformation near the South-East lakeshore that may be related to geothermal power production at location *A* indicated in Figure 4.5, and the tectonically related deformation feature running ~20 km in NW-SE direction on the west side of the Imperial Valley, associated with surface creep on the Superstition Hills Fault (B, in Figure 4.5). The deformation caused by the Superstition Hills Fault exhibits clear relative surface displacement across the fault, with a peak velocity of ~8mm/yr in the line-of-sight (LOS) direction. The cross-section profile B through the velocity field in 4.5 also reveals a clear displacement across the fault. The sign convention here is that positive velocity indicates increases in LOS distances, such that our data are consistent with right-lateral strike-slip motion on the Superstition Hills Fault.

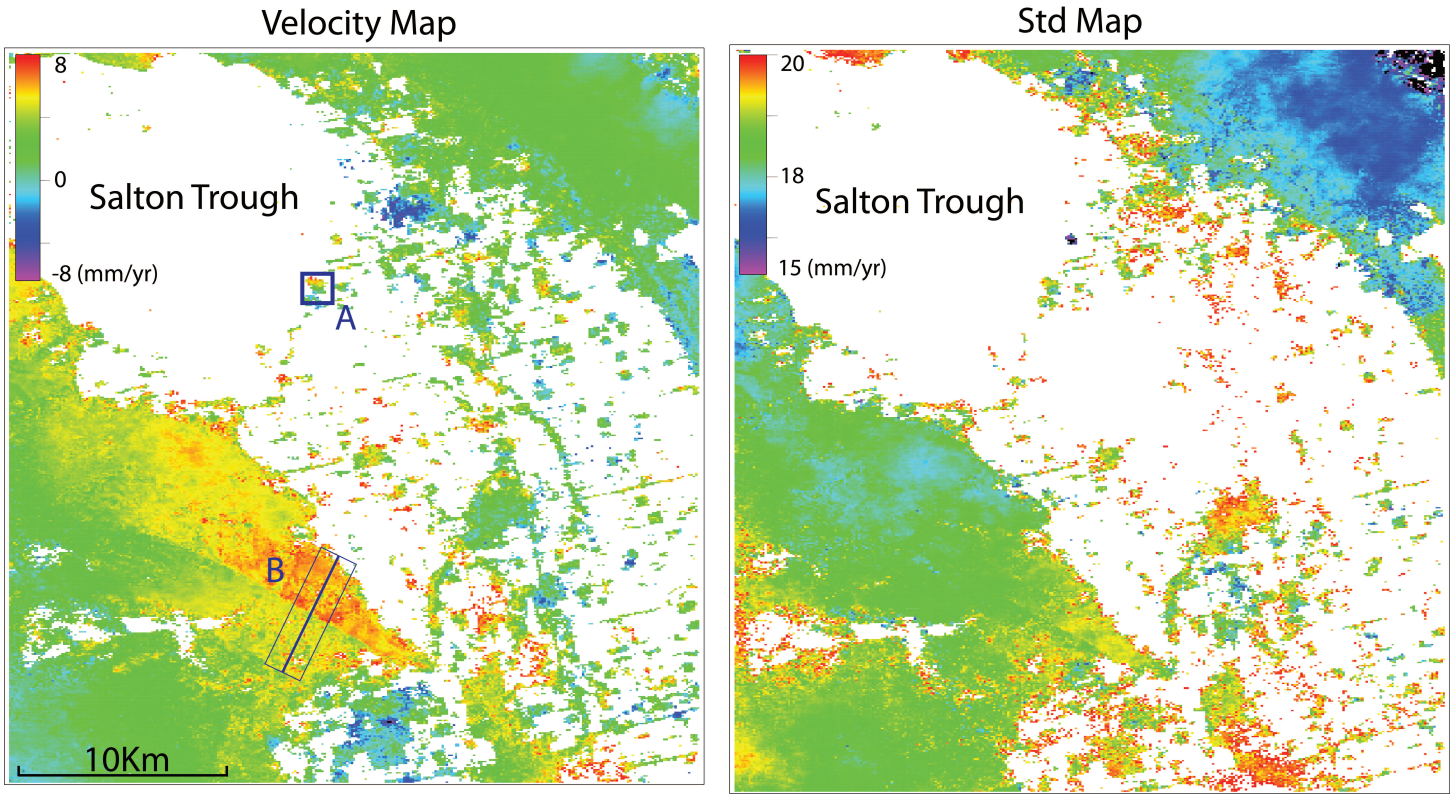

Figure 4.5: Left panel is our average velocity map, positive value (red) indicates increasing LOS distance (away from the satellite) and negative value (blue) indicates decreasing LOS distance (toward the satellite). Boxed region A indicates local subsidence potentially caused by geothermal power generation or extraction of groundwater. B indicates the profile crossing the Superstition Hills Fault shown in Figure 4.2. Right panel is the standard deviation map, indicating how the noise on our measurement of average velocity varies across the region.

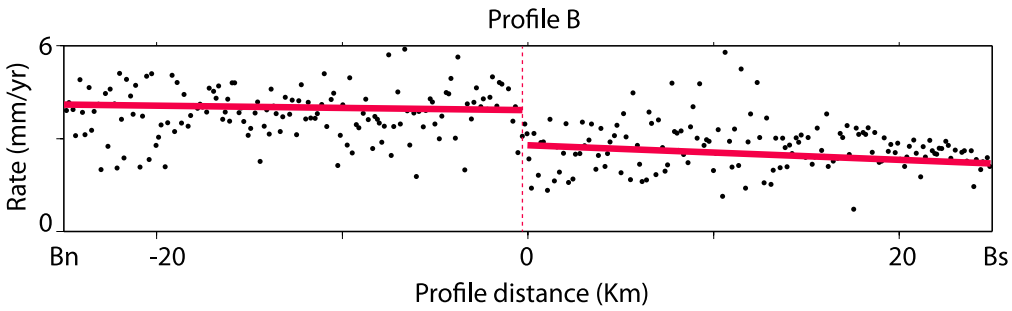

Figure 4.6: Deformation profile at B in Figure4.5. Red lines are the best fitting velocity on both sides of the faults. A clear dislocation can be observed.

We also observe a strong deformation gradient within a coherent region, near a known geothermal power plant as indicated by box A in Figure 4.5. The deformation time series is shown in 4.7, indicating a LOS deformation rate of ~13mm/yr between the two fastest moving regions.

4.3 Discussion and Future Prospects

We observe realistic deformation signals across the Superstition Hills Fault in our preliminary mean velocity map, providing good evidence for surface creep. However, the estimated velocities in the decorrelated regions in the valley have large errors, as were discussed in Chapter 2 and demonstrated with our synthetic tests.

The Imperial Fault has previously been mapped and the fault trace should be visible within the valley. However, our unwrapping results in the valley can be erroneous due to density of the coherent regions. Therefore, here I can only provide qualitative conclusion of the potential inversion resolution. The

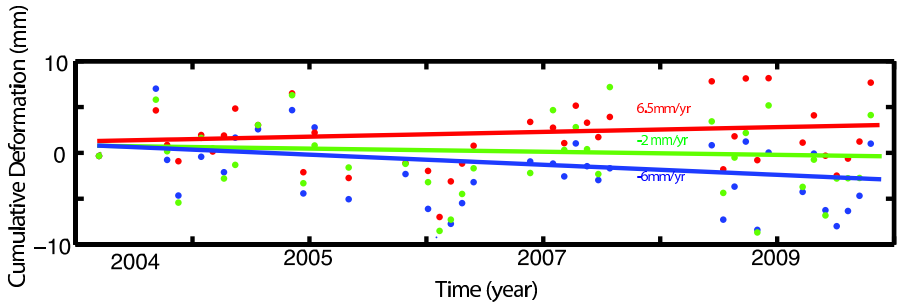

Figure 4.7: Deformation time series of A in figure 4.5. The deformation time series at three different locations within the deforming region are shown.

spatial density of data near the Imperial fault varies, which suggests variation in resolution along strike. The slip distribution at shallow depth can be robust since the inversion sensitivity is best at surface and poor at depth (Figure 3.6). The locking depth may be resolvable within a few kilometers. Our future work may involve synthetic tests using a 3-D fault plane and 2-D data to quantify the resolvable scale of lateral and vertical heterogeneity.

APPENDIX A

INTERFEROMETRY PROCESSING STRATEGY

The following flow chart provides a general InSAR processing strategy

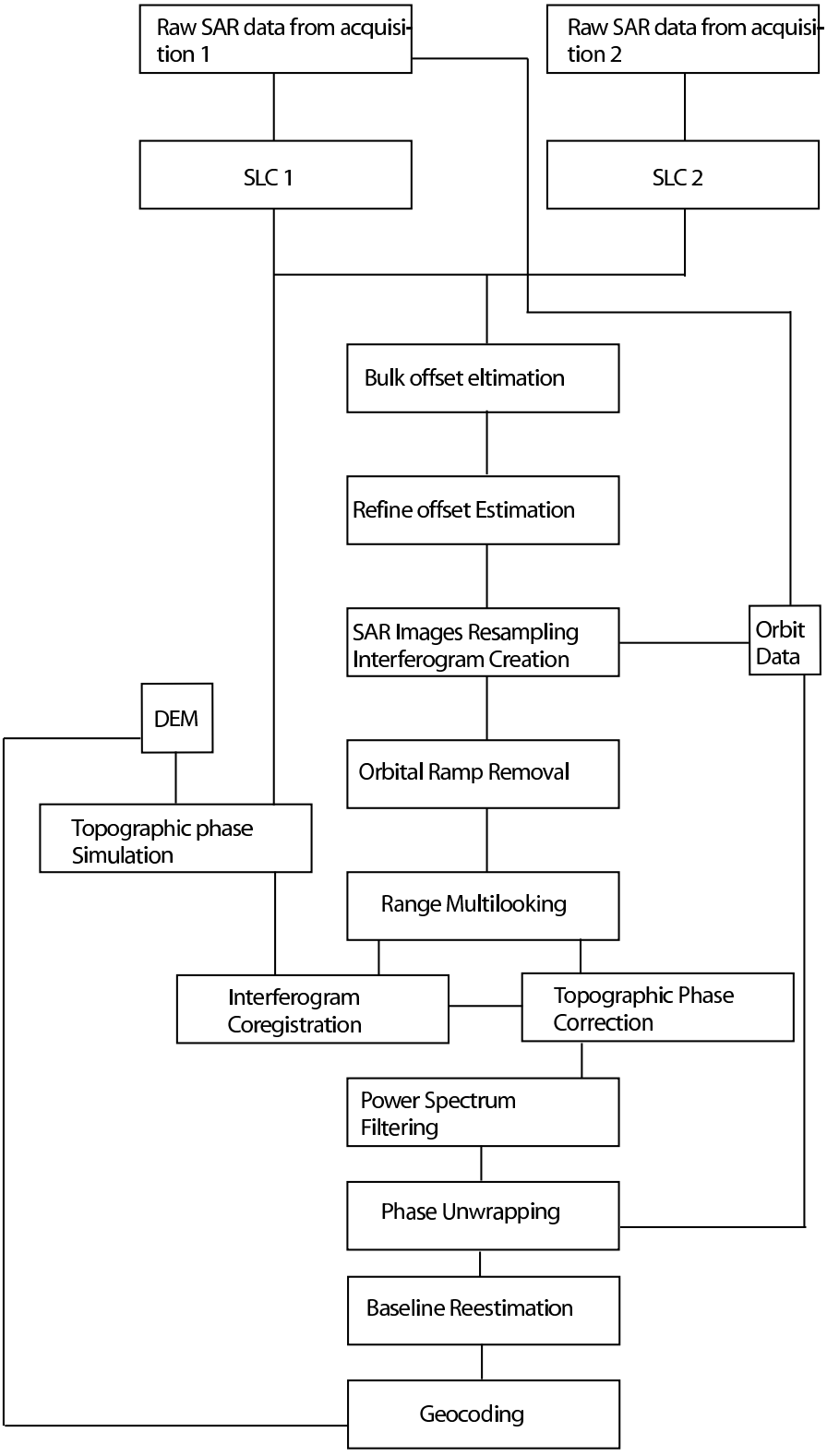
Raw SAR data from acquisition 1
Raw SAR data from acquisition 2
SLC 1
SLC 2
Bulk offset eltimation
Refine offset Estimation
SAR Images Resampling
Interferogram Creation
Orbit Data
DEM
Orbital Ramp Removal
Topographic phase Simulation
Range Multilooking
Interferogram Coregistration
Topographic Phase Correction
Power Spectrum Filtering
Phase Unwrapping
Baseline Reestimation
Geocoding

BIBLIOGRAPHY

Barnhart, W. D., and R. B. Lohman (2010), Automated fault model discretization for inversions for coseismic slip distributions, *Journal of Geophysical Research*, *115*(B10), 1–17, doi:10.1029/2010JB007545.

Bennett, R. A., W. Rodi, and R. E. Reilinger (1996), Global Positioning System constraints on fault slip rates in southern California and northern Baja, Mexico, *101*(96).

Berardino, P., G. Fornaro, R. Lanari, S. Member, and E. Sansosti (2002), A New Algorithm for Surface Deformation Monitoring Based on Small Baseline Differential SAR Interferograms, *40*(11), 2375–2383.

Brune, J. N., and C. R. Allen (1967), A low-stress-drop, low-magnitude earthquake with surface faulting: The imperial, california, earthquake of march 4, 1966, *Bulletin of the Seismological Society of America*, *57*(3), 501–514.

C. DeMets, l R. G. Gordon, D. F. A., and S. Stein (1994), Effect of recent revisions to the geomagnetic reversal time scale on estimates of current plate motion.

Chen, C., and H. Zebker (2002), Phase unwrapping for large sar interferograms: statistical segmentation and generalized network models, *Geoscience and Remote Sensing, IEEE Transactions on*, *40*(8), 1709 – 1719, doi:10.1109/TGRS.2002.802453.

Chen, C. W., and H. A. Zebker (2001), Two-dimensional phase unwrapping with use of statistical models for cost functions in nonlinear optimization, *18*(2), 338–351.

Du, Y., A. Aydin, and P. Segall (1992), Comparison of various inversion techniques as applied to the determination of a geophysical deformation model

for the 1983 borah peak earthquake, *Bulletin of the Seismological Society of America*, *82*(4), 1840–1866.

Emardson, T. R., F. H. W., M. Simons (2003), Neutral atmospheric delay in interferometric synthetic aperture radar applications: Statistical description and mitigation, *Journal of Geophysical Research*, *108*(B5), 1–8, doi: 10.1029/2002JB001781.

Farr, M., Tom G. ; Kobrick (2000), The Shuttle Radar Topography Mission.

Ferretti, a., C. Prati, and F. Rocca (2001), Permanent scatterers in SAR interferometry, *IEEE Transactions on Geoscience and Remote Sensing*, *39*(1), 8–20, doi: 10.1109/36.898661.

Ghiglia, D. C., and L. A. Romero (1994), Robust two-dimensional weighted and unweighted phase unwrapping that uses fast transforms and iterative methods, *11*(1), 107–117.

Glowacka, E., F. A. Nava, G. D. de Cosso, V. Wong, and F. Farfn (2002), Fault slip, seismicity, and deformation in mexicali valley, baja california, mexico, after the m 7.1 1999 hector mine earthquake, *Bulletin of the Seismological Society of America*, *92*(4), 1290–1299, doi:10.1785/0120000911.

Goldstein, R. M., and C. L. Werner (1998), Radar interferogram filtering for geophysical applications, *Geophysical Research Letters*, *25*(21), 4035, doi: 10.1029/1998GL900033.

Hansen, P. (1987), *Rank-Deficient and Discrete Ill-Posed Problems: Numerical Aspects of Linear Inversion*, Siam Monographs on Mathematical Modeling and Computation, SIAM.

Hill, D. P., P. Mowinckel, and L. G. Peake (1975), Earthquakes, active faults, and geothermal areas in the imperial valley, california, *Science*, *188*(4195), 1306–1308, doi:10.1126/science.188.4195.1306.

Hooper, A., H. Zebker, P. Segall, and B. Kampes (2004), A new method for measuring deformation on volcanoes and other natural terrains using InSAR persistent scatterers, *Geophys. Res. Lett.*, *31*(23), L23,611, doi: 10.1029/2004GL021737.

Jonsson, S., H. Zebker, P. Segall, and F. Amelung (2002), Fault slip distribution of the 1999 mw 7.1 hector mine, california, earthquake, estimated from satellite radar and gps measurements, *Bulletin of the Seismological Society of America*, *92*(4), 1377–1389, doi:10.1785/0120000922.

Kerrick, D. M., A. M. Michael, T. M. Seward, and K. Caldeira (1995), CHEMICAL GEOLOGY Convective hydrothermal C O 2 emission from high heat flow regions, *2541*.

Li, Z., E. J. Fielding, and P. Cross (2009), Integration of InSAR Time-Series Analysis and Water-Vapor Correction for Mapping Postseismic Motion After the 2003 Bam (Iran) Earthquake, *47*(9), 3220–3230.

Lohman, R. (2004), The Inversion of Geodetic Data for Earthquake Parameters, *Ph.D. thesis, California Institute of Technology*.

Lohman, R. B., and J. J. Mcguire (2007), Earthquake swarms driven by aseismic creep in the Salton Trough , California, *Earthquake*, *112*, 1–10, doi: 10.1029/2006JB004596.

Lyons, S. N., Y. Bock, and D. T. Sandwell (2002), Creep along the Imperial Fault,

southern California, from GPS measurements, *J. Geophys. Res.*, *107*(B10), 2249, doi:10.1029/2001JB000763.

Masterlark, T., C. DeMets, H. F. Wang, O. Snchez, and J. Stock (2001), Homogeneous vs heterogeneous subduction zone models: Coseismic and postseismic deformation, *Geophys. Res. Lett.*, *28*(21), 4047–4050, doi: 10.1029/2001GL013612.

Meade, B. J., and B. H. Hager (2005), Block models of crustal motion in southern California constrained by GPS measurements, *America*, *110*, 1–19, doi: 10.1029/2004JB003209.

Menke, W. (1989), *Geophysical Data Analysis: Discrete Inverse Theory*, International Geophysics Series, Academic Press.

Okada, Y. (1985), Surface deformation due to shear and tensile faults in a half-space, *Bulletin of the Seismological Society of America*, *75*(4), 1135–1154.

Richman (1971), Professional consulting services, *Spectrum, IEEE*, *8*(6), 91, doi: 10.1109/MSPEC.1971.5218168.

Rosen, P., S. Hensley, I. Joughin, F. Li, S. Madsen, E. Rodriguez, and R. Goldstein (2000), Synthetic aperture radar interferometry, *Proceedings of the IEEE*, *88*(3), 333 –382, doi:10.1109/5.838084.

Segall, P., and R. Harris (1987), Earthquake Deformation Cycle on the San Andreas Fault Near Parkfield, California, *Journal of Geophysical Research*, *92*(B10), 10,511–10,525, doi:10.1029/JB092iB10p10511.

Shearer, P. M. (2002), Parallel fault strands at 9-km depth resolved on the Imperial Fault , Southern California, *Geophysics*, *29*(14), 5–8.

Smith-Konter, B., and D. Sandwell (2009), Stress evolution of the San Andreas fault system : Recurrence interval versus locking depth, *Stress: The International Journal on the Biology of Stress*, *36*, 1–5, doi:10.1029/2009GL037235.

Thomas, P., and K. Rockwell (1996), Heber2, *101*, 5987–5997.

Tizzani, P., P. Berardino, F. Casu, P. Euillades, M. Manzo, G. Ricciardi, G. Zeni, and R. Lanari (2007), Surface deformation of Long Valley caldera and Mono Basin, California, investigated with the SBAS-InSAR approach, *Remote Sensing of Environment*, *108*(3), 277–289, doi:10.1016/j.rse.2006.11.015.

Zebker, H., and J. Villasenor (1992), Decorrelation in interferometric radar echoes, *Geoscience and Remote Sensing, IEEE Transactions on*, *30*(5), 950 –959, doi:10.1109/36.175330.

Zebker, H. A., S. Member, and J. Villasenor (1992), Decorrelation in Interferometric Radar Echoes, *30*(5), 950–959.

Zisk, S. H. (1972), Lunar topography: First radar-interferometer measurements of the alphonsus-ptolemaeus-arzachel region, *Science*, *178*(4064), 977–980, doi:10.1126/science.178.4064.977.